Geophysical Journal International

Geophys. J. Int. (2016) **207,** 1186–1202
Advance Access publication 2016 September 6
GJI Geodynamics and tectonics

doi: 10.1093/gji/ggw335

Dynamic topography, gravity and the role of lateral viscosity variations from inversion of global mantle flow

Ting Yang and Michael Gurnis

Seismological Laboratory, California Institute of Technology, Pasadena, CA 91125, *USA. E-mail: tyang@gps.caltech.edu*

Accepted 2016 September 2. Received 2016 September 1; in original form 2016 February 13

SUMMARY

Lateral viscosity variations (LVVs) in the mantle influence geodynamic processes and their surface expressions. With the observed long-wavelength geoid, free-air anomaly, gravity gradient in three directions and discrete, high-accuracy residual topography, we invert for depth- and temperature-dependent and tectonically regionalized mantle viscosity with a mantle flow model. The inversions suggest that long-wavelength gravitational and topographic signals are mainly controlled by the radial viscosity profile; the pre-Cambrian lithosphere viscosity is slightly (∼ one order of magnitude) higher than that of oceanic and Phanerozoic lithosphere; plate margins are substantially weaker than plate interiors; and viscosity has only a weak apparent, dependence on temperature, suggesting either a balancing between factors or a smoothing of actual higher amplitude, but short wavelength, LVVs. The predicted large-scale lithospheric stress regime (compression or extension) is consistent with the world stress map (thrust or normal faulting). Both recent compiled high-accuracy residual topography and the predicted dynamic topography yield ∼1 km amplitude long-wavelength dynamic topography, inconsistent with recent studies suggesting amplitudes of ∼100 to ∼500 m. Such studies use a constant, positive admittance (transfer function between topography and gravity), in contrast to the evidence which shows that the earth has a spatially and wavelength-dependent admittance, with large, negative admittances between ∼4000 and ∼10^4 km wavelengths.

Key words: Gravity anomalies and Earth structure; Mantle processes; Creep and deformation; Dynamics of lithosphere and mantle; Dynamics: convection currents, and mantle plumes; Rheology: mantle.

1 INTRODUCTION

Dynamic topography is the surface undulations induced by mantle flow (Pekeris 1935; Parsons & Daly 1983; Hager & Richards 1989) and plays an important role in geodynamics through a strong influence on the total topography (Zhong & Gurnis 1992; Faccenna *et al*. 2014), the long-term large-scale flooding history of continents (Lithgow-Bertelloni & Gurnis 1997), global and regional relative sea-level changes (Gurnis 1990; Moucha *et al*. 2008; Spasojevic & Gurnis 2012), and the amplitude and sign of the long-wavelength geoid (Hager & Richards 1989). Although the total topography of continents is dominated by the isostatic response of density variations within the crust and lithosphere and is mainly modulated by plate tectonics, changes in dynamic topography can significantly shift coastlines and change sediment and erosion patterns as large portions of continents are at elevations close to sea level (Flament 2014). Dynamic topography affects both relative and global sea levels over millions of years through the differential motion of continents over large-scale dynamic topography and through modulating ocean bathymetry. Through dynamic topography, long-term sea level variations as recorded on otherwise stable continental platforms are not a simple reflection of eustatic variations (Gurnis 1990; Moucha *et al*. 2008; Spasojevic & Gurnis 2012). Lateral variations of density within the mantle drive mantle convection, which further undulates mantle density interfaces (earth's surface, the core–mantle boundary, CMB, and any internal compositional interface). The long-wavelength gravitational field does not resemble surface topography, which is dominated by shallow density heterogeneity and modulated mainly by plate tectonics. Instead, it arguably reflects density heterogeneities inside the mantle and the corresponding dynamic topography (Hager & Richards 1989).

Given the importance of dynamic topography, attempts have been made to observationally constrain its geographical pattern and amplitude. The most common way to constrain dynamic topography has been to remove the isostatic signal from the observed total topography (Crough 1978; Wheeler & White 2000, 2002; Gurnis *et al*. 2000a; Panasyuk & Hager 2000b; Kaban *et al*. 2004; Czarnota *et al*. 2013; Becker *et al*. 2014; Winterbourne *et al*. 2014). The residual component of the topography cannot be accounted for by density heterogeneity within the crust and lithosphere (Crough 1978) and is often thought of as reflecting dynamic topography. Since the early explicit calculations of dynamic topography (Ricard *et al*. 1984;

Hager *et al*. 1985), there have been considerable discussions as to its amplitude. Numerical and laboratory experiments often predict large amplitude (1–2 km) dynamic topography (Ricard *et al*. 1993; Steinberger 2007; Conrad & Husson 2009; Husson *et al*. 2012; Flament *et al*. 2013). On the other hand, estimates of the amplitude of residual topography are more ambiguous, with some authors (Wheeler & White 2000, 2002; Kaban *et al*. 2004) arguing for small amplitudes (close to zero) of residual topography while others for much larger amplitudes (Crough 1978; Davies & Pribac 1993; Gurnis *et al*. 2000a; Panasyuk & Hager 2000b). This inconsistency between residual and dynamic topography is due to a variety of factors, including: (1) model assumptions of the cooling oceanic lithosphere, (2) large uncertainties in deciphering shallow density distributions in generating residual topography, and (3) uncertainty in the mantle density and viscosity structures which control mantle flow and dynamic topography.

Recently, several studies (Czarnota *et al*. 2013; Winterbourne *et al*. 2014; Hoggard *et al*. 2016) have attempted to recover residual topography on normal ocean floor at discrete locations (which we call point measurements) using previously acquired seismic reflection and refraction profiles (many from oil exploration) that yield accurate sediment and crustal thickness corrections. The amplitude of the new estimated residual topography is in excess of 1 km, close to the amplitude of dynamic topography from mantle convection models. However, based on the analysis of GTR (free-air gravity/residual topography ratio), the investigators (Winterbourne *et al*. 2014; Hoggard *et al*. 2016) suggest that the amplitude of the long-wavelength dynamic topography is small and the measured residual topography mainly arises from density variations immediately beneath the lithosphere.

GTR (free-air gravity/residual topography ratio) has long been used to estimate the compensation depth of surface topography (McKenzie 1977, 1994; Simons *et al*. 1997; Jones *et al*. 2012), assuming higher GTR corresponds to deeper mass compensation. GTR arising from mantle flow was often assumed to be constant with a value of ∼30 mGal km^{-1} (or ∼50 mGal km^{-1} on land) (Crosby *et al*. 2006; Crosby & McKenzie 2009; Molnar *et al*. 2015). Based on the band-pass filtered (700–12 400 km) free-air gravity and their compiled high-accurate residual topography, Winterbourne *et al*. (2014) inferred that the GTR for the residual topography is ∼22 mGal km^{-1}. Because this is smaller than the 30 mGal km^{-1} commonly assumed to correspond to mantle convection (Crosby & McKenzie 2009), they suggested that most of the residual depth anomalies are caused by density heterogeneity within the uppermost mantle. In addition, Molnar *et al*. (2015) questioned the existence of dynamic topography based on the small amplitude of long-wavelength free-air and isostatic gravity anomalies. For example, Molnar *et al*. (2015) suggest that the amplitude of dynamic topography in several regions (e.g. southern Africa, Colorado Plateau) is less than ∼100 m, contrary to predictions from dynamic models that use seismic tomography inputs while attempting to fit the long-wavelength non-hydrostatic geoid (Hager *et al*. 1985; Ricard *et al*. 1993; Thoraval & Richards 1997; Gurnis *et al*. 2000a; Steinberger 2007; Conrad & Husson 2009; Flament *et al*. 2013). Recently, Hoggard *et al*. (2016) transformed onshore free-air gravity to residual topography assuming that the GTR is 50 mGal km^{-1}. Combining their onshore model of dynamic topography with compiled offshore residual topography, they argue that the amplitude of the long-wavelength dynamic topography is smaller than 500 m.

Dynamic topography depends on mantle viscosity, one of the key controls on GTR (Hager 1984; Colli *et al*. 2016). Laboratory experiments on rock deformation suggest that mantle viscosity depends strongly on temperature (Karato & Wu 1993) such that cold slabs (and hot upwelling flow) might be orders of magnitude stronger (weaker) than the surrounding mantle. Such strong lateral viscosity variations (LVVs) may affect mantle flow and surface observations significantly (Moresi & Gurnis 1996; Zhong & Davies 1999; Zhong *et al*. 2000; Čadek & Fleitout 2003; Stadler *et al*. 2010). For example, temperature-dependent viscosity stiffens cold downwellings while enhancing the ability of cold slabs to penetrate through the 660 km endothermic phase boundary (Zhong & Gurnis 1994; Zhong *et al*. 2000). On the other hand, temperature-dependent viscosity weakens the hot upwelling while reducing the ability of plumes to penetrate through the 660 km endothermic phase boundary (Zhong *et al*. 2000). Observations show that the long-wavelength (e.g. degree 4–9) geoid is high over subduction zones (Chase 1979; Hager 1984). In radially layered viscosity models, this is explained by a one to two orders of magnitude viscosity jump across the 660 km discontinuity, which leads to a smaller downward deflection of surface topography at subduction zones such that the slab density increase has more contribution to the geoid than the surface topographic depression does (Hager 1984; Hager & Richards 1989; Ricard *et al*. 1993; Panasyuk & Hager 2000a; Soldati *et al*. 2009). A stiffened slab through the temperature dependence of viscosity, on the other hand, can lead to larger deflections of the surface compared to that with just radial viscosity variations and in turn lead to a negative geoid anomaly over subduction zones or the inference of even larger jumps in viscosity between the upper and lower mantle (Moresi & Gurnis 1996).

Bounds on LVVs remain poorly established and most previous studies limit inversion to 1-D (depth-dependent) mantle viscosity (King 1995; Panasyuk & Hager 2000a; Mitrovica & Forte 2004; Soldati *et al*. 2009; Rudolph *et al*. 2015). Several studies computed instantaneous mantle flow and investigated the influence of LVVs on geodynamic processes and surface observations (Moresi & Gurnis 1996; Zhong & Davies 1999; Tosi *et al*. 2009). These studies indicate that the strong slab generates low geoid around subduction zones, inconsistent with observed geoid highs and suggested that the cold slab in the mantle might be significantly weakened compared with that inferred from temperature-dependent viscosity. In contrast, other studies (Moucha *et al*. 2007; Ghosh *et al*. 2010) suggest that LVVs have only a weak influence on surface observations. These forward calculations added the LVVs to pre-inverted 1-D radial viscosity profiles and consider their effects on surface observations. However, LVVs and the radial viscosity profile are likely coupled and their influence on observations remains to be investigated through the simultaneous inversion of these parameters. For example, through the temperature-dependence of viscosity, prolonged subduction regionally may give rise to a strong radial gradient between the upper and lower mantle as well as a lateral gradient between the normal mantle and strong slabs. A somewhat opposite situation may be associated with the large-scale upwellings associated with the large low shear velocity provinces in the lower mantle. LVVs related to these cold slabs and hot upwellings are expected to affect surface observations (Moresi & Gurnis 1996; Zhong & Davies 1999; Zhong *et al*. 2000; Čadek & Fleitout 2003). Ghosh *et al*. (2010, 2013) computed numerous forward models and tried to adjust both lateral and radially viscosity parameters manually to fit both the geoid and surface plate motion. However, formal inversions for viscosity parameters and investigations on their trade-offs are needed to better understand the viscosity structure of the mantle.

This paper has several aims. We invert for depth- and temperature-dependent and tectonically regionalized mantle viscosity driven by

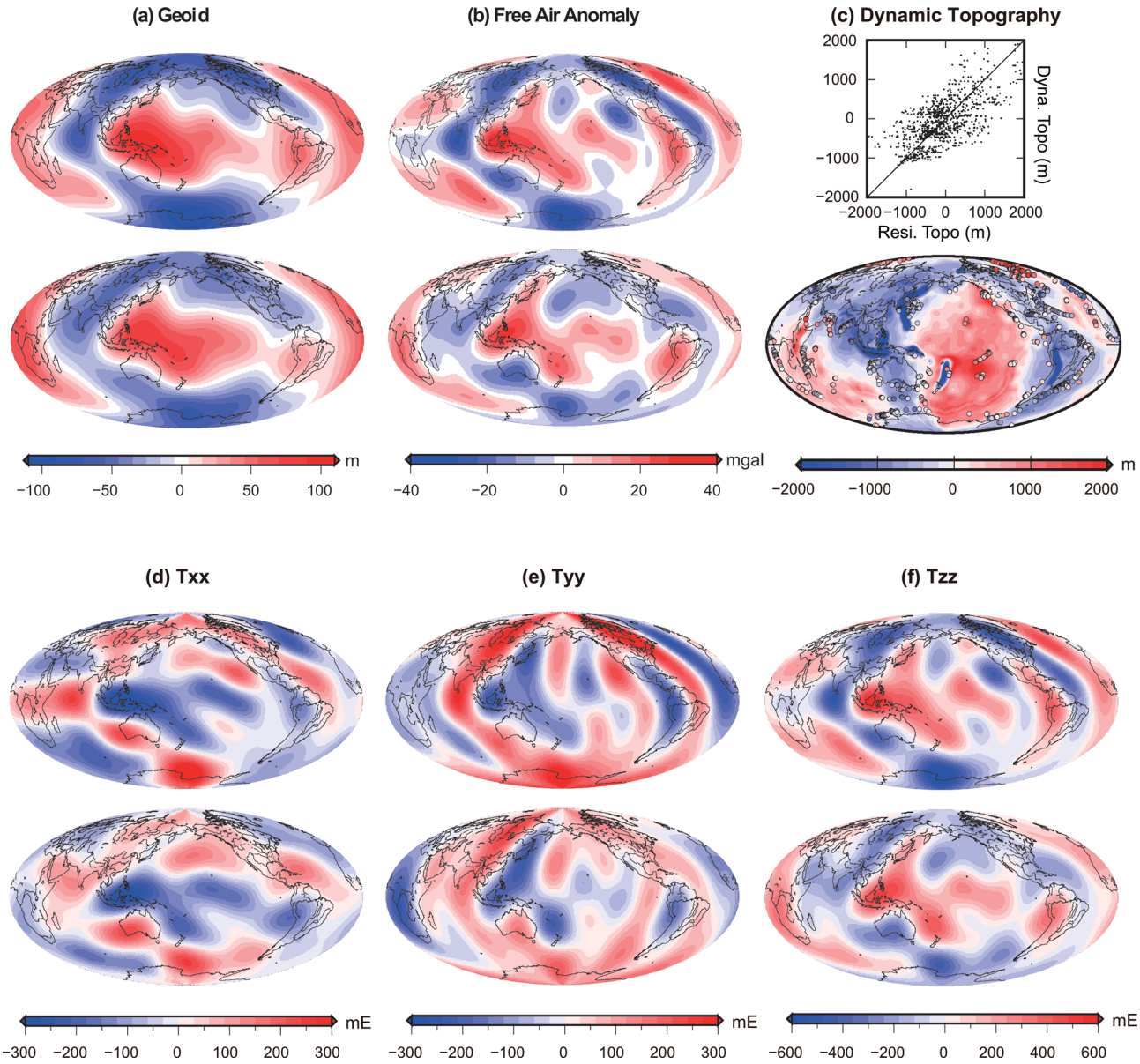

Figure 1. Observed (upper) and predicted (lower) geoid (a), free-air anomaly (b) and gravity gradients in the north (d), west (e), and radial (f) directions. (c) Dynamic topography versus residual topography at residual topography observation points (upper) and map view of dynamic topography (bottom) overlaid by 1006 high-accuracy residual topography at discrete observation points (Hoggard *et al*. 2016).

mismatches between the observed and predicted non-hydrostatic geoid, free-air gravity, gravity gradients and discrete values of residual topography (Fig. 1). In addition, we investigate the relationship between free-air gravity and dynamic topography as a function of wavelength and investigate the possibility that the observed free-air gravity anomalies and the putative large amplitude long-wavelength dynamic topography can be reconciled by a dynamic model. Although there have been numerous studies on this topic, here we use the gradient of the gravity along with the newly available discrete residual topography observations in an inversion. We verify that the predicted dynamic topography and high-accuracy observed residual topography are consistent in both pattern and amplitude at long-wavelengths. We also investigate the structure of LVVs, their trade-offs, and influence on surface observations.

2 METHOD

We constrain mantle structure with the long-wavelength (degree 2–8) geoid, free-air anomaly, gravity gradients, and recently compiled point measurement of residual topography. We choose only the long-wavelength (spherical degree $\leq$8) gravitational fields as constraints on the inversion because (1) Global seismic tomography models from different groups based on different datasets and different processing techniques are generally consistent for those wavelengths but generally inconsistent over the globe for shorter wavelengths; (2) The effects of shallow density heterogeneities on the gravitational fields cannot be neglected for wavelengths shorter than ~degree 8 (Richards & Hager 1988). Although the geoid, free-air anomaly, and gravity gradients are all derived from the gravitational field, they are sensitive to mantle structures over different depth and length

scales. It has also recently been suggested that the gravity gradients (e.g. from the GOCE, Gravity field and steady-state Ocean Circulation Explorer, mission) provide additional constraints on mantle structure and dynamics (Panet *et al*. 2014). The zonal coefficients of the hydrostatic (Chambat *et al*. 2010) and coefficients of incomplete postglacial rebound (Geruo *et al*. 2013) have been subtracted from the GOCE (Reguzzoni & Tselfes 2009) geopotential models to reveal a gravitational signal putatively related to mantle flow. Geruo *et al*. (2013) load a compressible, viscoelastic earth with the ICE-5 G global ice loading history and then infers the glacial isostatic adjustment and the present-day gravitational signals due to the incomplete postglacial rebound. Compared to the Nakiboglu (1982) hydrostatic Earth model, the Chambat *et al*. (2010) model yields a more oblate non-hydrostatic geoid, with the geoid at the equator higher than that using the Nakiboglu correction. However, the inverted mantle structure is not significantly affected by changes in the hydrostatic model. The residual topography data (Czarnota *et al*. 2013; Winterbourne *et al*. 2014; Hoggard *et al*. 2016), although sparse, provides important data for the inverse approach. Besides the above observations, smoothed (Koptev *et al*. 2013) stress regime (compression or extension) based on a recent compilation of the world stress map (Heidbach *et al*. 2010) is compared to our predicted average lithospheric horizontal stress (negative or positive). Since the stress regime observation is not applied in the inversion, it provides independent verification of model outcome.

The cost function of our inversion is

$$J = \sqrt{\frac{\sum (N^p - N^o)^2}{N_C}} + w_F \sqrt{\frac{\sum (F^p - F^o)^2}{N_C}} + w_z \sqrt{\frac{\sum \left(U_{zz}^p - U_{zz}^o\right)^2}{N_C}} + w_x \sqrt{\frac{\sum \left(U_{xx}^p - U_{xx}^o\right)^2}{N_C}} + w_y \sqrt{\frac{\sum \left(U_{yy}^p - U_{yy}^o\right)^2}{N_C}} + w_D \sqrt{\frac{\sum (H^p - H^o)^2}{N_D}} \quad (1)$$

where N, F, U_{zz}, U_{xx}, U_{yy} are geoid height, free-air anomaly, vertical, north and west direction gravity gradients at CitcomS grid points, respectively. The CitcomS grid points are distributed in an equal area fashion across the globe (see Zhong *et al*. 2000). Superscript p and o represent predicted and observed values respectively. H is the topography (where the predicted value is dynamic topography and the observed value the residual topography) at the residual topography observation points. N_C and N_D are the numbers of CitcomS grid and residual topography observation points, respectively. w is the weight for each quantity. The goodness of fit between the predicted and observed gravitational fields is expressed as residuals at discrete uniformly distributed grid points instead of spherical harmonic correlations (Ghosh *et al*. 2010). The spherical harmonic correlation method is sensitive to the pattern of the gravitational field but does not include the amplitude information. Previous studies with only the geoid as constraints report slightly different inverted results for different goodness of fit calculating methods (Rudolph *et al*. 2015). However, the choice of methods to calculate the goodness of fit does not influence our inversion as we explicitly incorporate residual topography as constraints in the inversion. With the weight of the geoid set to unity, the weights of other quantities are set to the ratios of the amplitudes of the geoid (∼100 m) and that of each quantity. For example, the amplitude of long-wavelength free-air gravity anomaly is ∼30–50 mGal and we give it a weight of 2. Weights of the gravity gradients along three orthogonal directions are divided by three to ensure that the gravity gradient observations are not overly weighted. The weight for free-air gravity, vertical, north and west direction gravity gradients, and dynamic topography terms are set to 2, 0.0333, 0.0667, 0.0667 and 0.03, respectively. Although we have three kinds of gravity observations and one kind of residual topography observation, we do not multiply the weight of residual topography by three because (1) geoid, free-air anomaly, and gravity gradients are sensitive to different depth and wavelength of the mantle; (2) among all the observations, residual topography may be the least accurate; and (3) small variations of the weights (e.g. increasing the weight of free-air gravity to 3 or reducing it to 1 or doubling the weight of dynamic topography) do not strongly influence the inverted results.

We use Powell's method (Press *et al*. 2007) to invert for model parameters. Starting from an initial guess of each of the N model parameters, Powell's method sequentially optimizes the parameters in each direction to find the minima of an N-variables cost function (Fig. 2a). Powell's method does not calculate the gradient of the cost function to get the search direction. Calculating the gradient of the cost function requires solving the Stokes equations, which is time-costing and prevents the use of gradient methods (e.g. conjugate gradient method). The Powell's method finds only the local minima (Press *et al*. 2007). In contrast, probabilistic methods (such as simulated annealing, genetic or neighbourhood algorithms), which also do not require the gradient of the cost function, can be used to avoid falling into local minima. However, probabilistic methods usually require many more iterations than Powell's while strongly relying on the user's experience and do not always ensure finding the global minimum (Sen & Stoffa 2013). For example, simulated annealing requires setting up what is called an annealing schedule (initial temperature, temperature reduction rate, acceptance probabilities; Van Laarhoven & Aarts 1987) to maximize the probability of convergence on the global minimum within a limited computational time (Sen & Stoffa 2013). However, there are no universal rules for setting up the annealing schedule and different problems usually require different annealing schedules. Although Powell's method only finds local minima of the cost function, we attempt to avoid this problem by performing Powell's inversion several times with randomly chosen initial parameters and parameter searching orders. This can be regarded as a hybrid of Powell's and a probability method as it attempts to incorporate both the advantages of Powell's method, which can find the local minima rapidly, and a probability method that tries to find the global minimum. The inversion terminates either if the decrease of the solution between two outer iterations (optimizing the cost function sequentially in each direction) of the Powell method is less than 0.01 or the number of outer iterations exceeds 10.

For each one-direction optimization problem, the traditional Powell's method tries to find the global minimum in this direction (Press *et al*. 2007). This usually asks for a large number of forward calculations. In contrast, we use a method similar to inverse quadratic interpolation (Press *et al*. 2007) to find only the approximate global minimum. That is, we use a second order polynomial to fit the cost function at three discrete points (one is passed on from the last iteration) and then use this polynomial to predict the position of the optimal point. After evaluating the cost function at this predicted optimal point, we choose the point of the minimal cost function among those four points as the optimal solution for the one-directional optimization problem. After each outer loop of Powell's method, we reduce the search radius of each search direction. This setup enables us to find the global minimum for the N-variable cost function

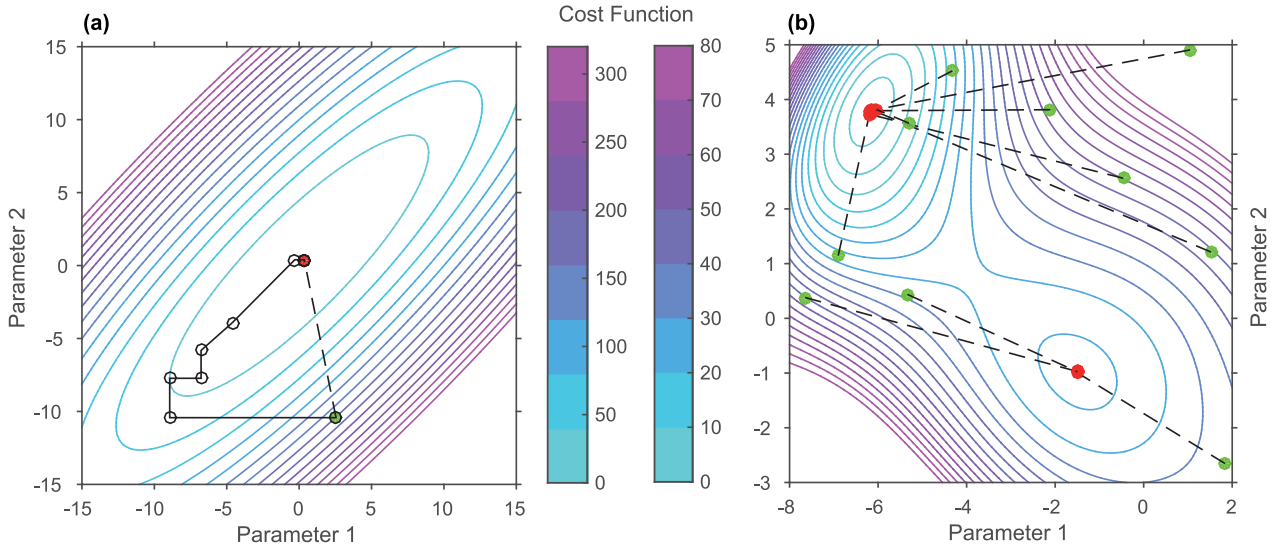

Figure 2. (a) Sequence of accepted points generated by Powell's method for a 2-D optimization problem. (b) Optimization for a two variable cost function with multiple local minima. Our inversion strategy finds the global minimum. Colour lines in (a) and (b) represent contour lines of the cost function. Green and red points represent the initial guess and inverted parameters, respectively. Open circles in (a) represent the optimal value of each one-direction search.

Table 1. Constant physical parameters.

Parameters	Value
Reference mantle density	3.3e3 kg m^{-3}
Air density	0 kg m^{-3}
Water density	1.0×10^3 kg m^{-3}
Gravitational acceleration	9.8 m s^{-2}
Thermal expansivity	3×10^{-5} °C^{-1}
Reference temperature	2500 °C
Mantle depth	2867 km
Thermal diffusivity	1×10^{-6} m^2 S^{-1}

efficiently. We have conducted two synthetic tests (Figs 2a and b) to verify this method. For the problem with only one minimum in the parameter space (Fig. 2a), Powell's method finds the global minimum rapidly. For a problem with multiple minima (Fig. 2b), we run Powell's method ten times, each with different initial guesses and parameter searching orders. Seven find the global minimum while the others find the local minima.

We use the finite element method in a spherical shell, CitcomS (Zhong *et al*. 2000), to calculate mantle flow and related surface observations assuming the Boussinesq approximation. CitcomS enables the inclusion of LVVs which arise from temperature-dependent and tectonically regionalized viscosities in the calculation. We use a mesh of 65^3 in each of twelve approximately equal-area caps with vertical refinement in the upper mantle. This resolution is compatible with that of the tomography model (Ritsema *et al*. 2011) and RUM (Gudmundsson & Sambridge 1998) slab model that were used to construct the buoyancy field. For the best-fitting model, we re-compute the flow and predictions with a mesh resolution of $129 \times 129 \times 65$ and between different resolutions we find negligible (less than 1 per cent) difference for all of the representations associated with the gravitational field and topography. Physical constants used in this study are listed in Table 1.

The non-dimensional, depth- and temperature-dependent and tectonically regionalized viscosity is expressed as

$$\eta = \eta_0 \eta_t f\left(\varepsilon_{\amalg}\right) \exp\left[-E\left(T - T_0\right)\right], \tag{2}$$

where η_0, η_t, E and T_0 are viscosity pre-factor for each layer, regional (tectonic) viscosity contrast, non-dimensional activation energy and reference temperature within each layer, respectively. T is the non-dimensional temperature, which varies continuously. The mantle is divided into four layers: lithosphere, upper mantle, transition zone and lower mantle, each with their own viscosity parameters. The reference temperature is set to 0.5 for all layers. The lithosphere is divided into oceanic, Phanerozoic, pre-Cambrian and plate margins each of which has a different viscosity (Figs 3a and b), as defined by η_t. η_t of the oceanic lithosphere is set to unity, meaning that we use the average oceanic lithosphere viscosity to represent the viscosity pre-factor of the lithosphere layer. Below the lithosphere, η_t is set to 1. The viscosity of the plate margins is assumed to depend on the second invariant of the strain rate tensor from the Global Strain Rate Map (GSRM; Kreemer *et al*. 2003), in which diffuse plate boundaries are included. In plate margins, viscosity reduces with the increase in strain rate:

$$f(\varepsilon_{\amalg}) = \frac{1}{\eta_t} - \frac{(1-\eta_t)\log(\varepsilon_{\amalg}/\varepsilon_{\amalg\ \mathrm{Min}})}{\eta_t \log\left(\varepsilon_{\amalg\ \mathrm{Max}}/\varepsilon_{\amalg\ \mathrm{Min}}\right)}, \tag{3}$$

where $\varepsilon_{\amalg}$ is the second invariant of the strain rate tensor. Min and Max represent the minimum and maximum values of the strain rate invariant from GSRM. The plate margin viscosity increases from η_t at the maximum strain rate to surrounding mantle viscosity at the minimal strain rate (Fig. 3b). The quantities (gravitational fields and residual topography) only allow us to constrain the relative viscosity variations. So we fix the non-dimensional viscosity at the reference temperature in the lower mantle to unity and invert for viscosity parameters. Inverted (best fit) viscosity parameters are listed in Table 2.

Assuming purely thermal convection, the horizontal mantle temperature perturbation (Fig. 3c), which drives mantle flow, is constructed from a combination of a smooth seismic velocity model (S40RTS; Ritsema *et al*. 2011) and a discontinuous slab model (RUM; Gudmundsson & Sambridge 1998). The inverted viscosity structures are not changed if we use the smoothed tomography model for the whole mantle. The viscosity structure derived from

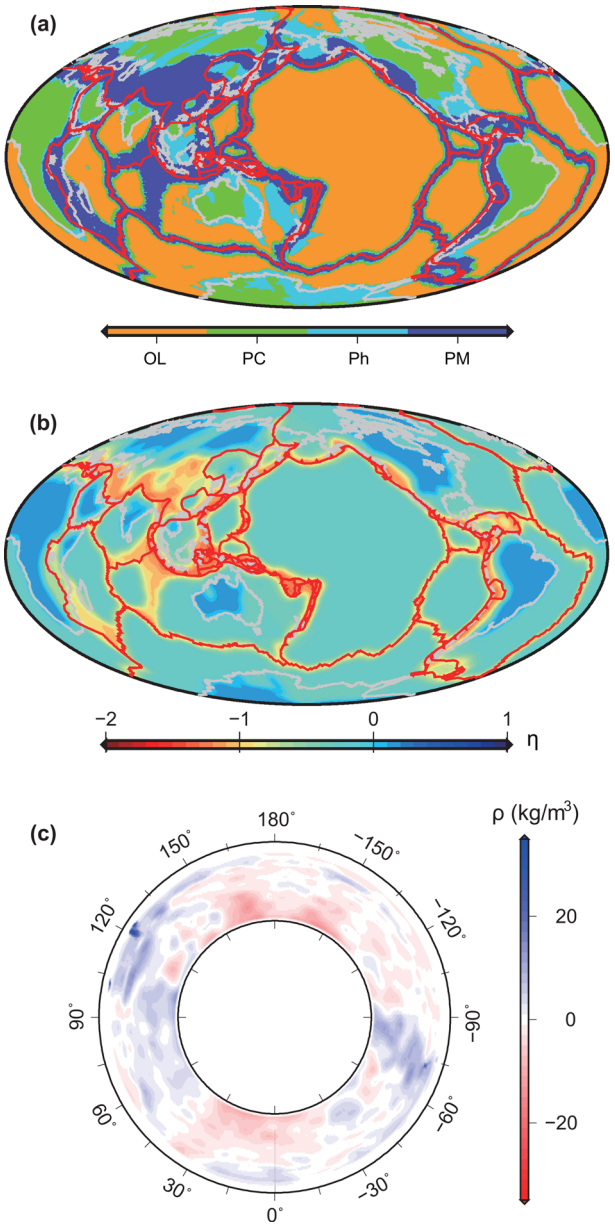

Figure 3. (a) Tectonic provinces that each has a different viscosity. OL, PC, Ph, and PM represent oceanic lithosphere, pre-Cambrian continental lithosphere, Phanerozoic continental lithosphere and plate margins (including diffuse zones), respectively. (b) Inverted 3-D mantle viscosity (Table 2) at 91 km depth. The pre-Cambrian lithosphere is stiffer than the Phanerozoic and oceanic lithospheres and plate margin region is much weaker than plate interiors. (c) Inverted mantle density perturbation along the equator.

these inversions is close to the combined density model. Density, and hence temperature, variations within the upper 250 km associated with S40RTS are ignored because (1) the relationship between density and seismic perturbation is complex in the shallow mantle (Deschamps *et al*. 2001). The large variations of temperature and composition of the uppermost mantle seem to balance each other to a large degree (Jordan 1975). For example, Mg# and Fe/Al depletion and temperature reduction of the subcontinental lithospheric mantle result in a seismically high velocity continental lithosphere while being neutrally buoyant (Djomani *et al*. 2001); and (2) at long wavelengths the effect of shallow density heterogeneities on the geoid is less than ∼10 m (Richards & Hager 1988). We first fix dT/dV_s, the ratio between the non-dimensional temperature and shear wave velocity perturbation to that predicted by mineral physics (Karato & Karki 2001) for MgO and $MgSiO_3$ perovskite and invert for mantle viscosity only. After the mantle viscosity inversion, we also invert for dT/dV_s ratios within each layer for our preferred mantle viscosity structure.

3 RESULTS

3.1 Recovered viscosity

We verify our method of recovering mantle viscosity parameters. We first compute a forward model with known viscosity parameters (thick dashed red lines in Fig. 4) and then added 10 per cent Gaussian-distributed noise to the computed gravitational spherical harmonics coefficients and 500 m Gaussian distributed noise to dynamic topography at the residual topography observation points. Then, we attempted to recover the parameters with our inversion method. We performed Powell's procedure eight times with randomly assigned initial guesses of model parameters and search orders. Each operation of Powell's inversion requires a few hundred forward evaluations to yield the optimal viscosity parameters. The viscosity parameters best fitting the data are close to those of the input (Fig. 4) in nearly all cases. Viscosity models corresponding to the lowest one (ten) per cent of the cost function are highlighted with the green (yellow) lines in Fig. 4. Note that the yellow and green lines are not continuously distributed because of the limited sampling of the model space. Our updated Powell's method jumps from one point to another to find the optima. Increasing the number of sampling can make the green and yellow lines more continuous. However, the best solution is less influenced. The scatter of the green or yellow lines for inferred depth-dependent viscosity parameters is narrow, indicating that the radial profile is generally well recovered. The scatter of the inferred LVVs parameters is wider compared to depth-dependent viscosity parameters, indicating that LVVs are less well recovered by the long-wavelength surface observations. For example, the input Phanerozoic continental lithosphere viscosity contrast (Phanerozoic continental lithosphere/oceanic lithosphere viscosity ratio) is 2, however, models with viscosity contrasts of 1 or 10 also fit the observations as well, because variations in radial viscosity affect free-air anomaly globally while inclusions of LVVs affect free-air gravity regionally. Because the width of plate margins are generally narrow compared to long-wavelength observations (Fig. 3), the surface observations are also less sensitive to viscosity reduction in plate margins compared to radial viscosity profiles, as shown earlier from 2-D forward, instantaneous models of subduction (King & Hager 1994). However, the LVVs do affect the amplitude of dynamic topography and gravitational fields (King & Hager 1994; Moresi & Gurnis 1996) and our inversion strategy can recover the LVVs (Fig. 4), although with large uncertainty.

It has been suggested that gravity gradients provide extra constraints on mantle structure and dynamics (Panet *et al*. 2014). We conduct an additional synthetic inversion test, in which the gravity gradients are removed as constraints, to investigate the extra information provided by gravity gradients to the mantle viscosity inversion. The inverted mantle viscosity structure is similar to that in Fig. 4. But the inverted values for the tectonically related viscosity parameters are more scattered compared to when the gravity gradients are included (Fig. 4), suggesting that the gravity gradients do provide some limited additional constraints (Greff-Lefftz *et al*. 2016), especially on shallow structures.

Table 2. Inverted (best fit) viscosity parameters.

Viscosity pre-factor η_0		Viscosity contrast η_t		Non-dim activation energy E	
Depth (km)	Value	Type	Value	Depth (km)	Value
0–100	0.61	PM	0.019	0–100	0 (fixed)
100–410	0.17	Ph	0.90	100–660	−6.8
410–660	0.005	PC	7.5	660–2867	−13.1
660–2867	1 (fixed)				

Note: Viscosity contrast is the viscosity ratio of each type of lithosphere to the oceanic lithosphere. PM, PC and Ph denote plate margin, pre-Cambrian and Phanerozoic lithosphere respectively.

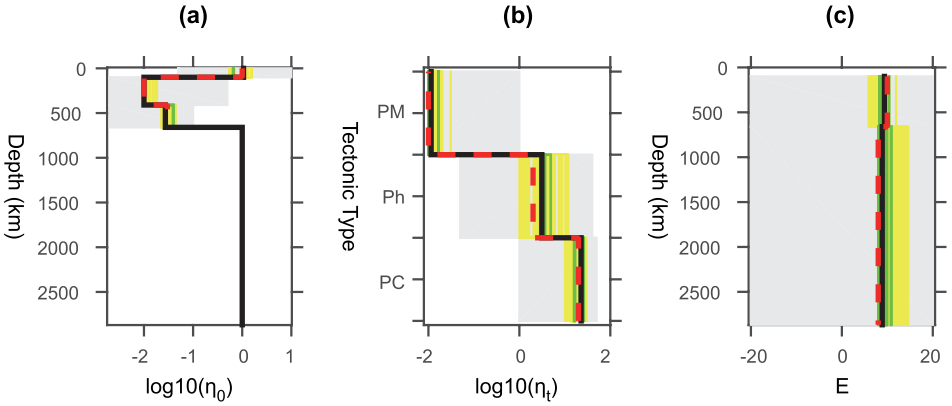

Figure 4. Synthetic test of the inversion method. (a) Recovered viscosity pre-factor of each layer. (b) Recovered viscosity contrast of each tectonic province relative to oceanic lithosphere. PM, PC and Ph denote plate margin, pre-Cambrian and Phanerozoic lithosphere, respectively. (c) Recovered activation energy of each layer. Red dash lines represent the input parameters of the synthetic model. Black lines represent the best-fit model. Yellow and green lines represent the best 1 and 10 per cent models. Grey regions denote the space that parameters were searched over.

As a reference to better understand our ability to recover lateral variations in viscosity, we first attempt to invert for a 1-D (depth-dependent) viscosity profile from the observed fields. The mantle is divided into four viscosity layers: the lithosphere, upper mantle, transition zone and lower mantle. With viscosity of the lower mantle fixed, we invert for viscosity of the other three layers. We performed Powell's inversion eight times with randomly assigned initial guesses of model parameters and search orders. Compared to the fixed viscosity of the lower mantle, the preferred radial viscosity profiles have a low viscosity upper mantle and transition zone and a high viscosity lithosphere with the viscosity about the same as the lower mantle (Fig. 5a), similar to previous studies (Hager & Richards 1989; King 1995; Panasyuk & Hager 2000a; Soldati *et al.* 2009). The inversion yields an upper-mantle viscosity higher than that in the transition zone. Although not a profile normally found or assumed with forward models, such profiles have previously been found from inverse studies (King 1995; Soldati *et al.* 2009). Reducing the viscosity in the upper mantle slightly will further reduce the coupling between the lithosphere and mantle below and reduce the amplitude of dynamic topography and geoid compared to the inverted model (Hager & Richards 1989).

To investigate how many layers the inversion can resolve, we also invert for two other models with different parameterizations of the viscosity layers for the 1-D model. One is a three-layer model, which combines the upper mantle and transition zone in the four-layer model (Figs 5a and b). The inversion yields a high viscosity lithosphere and lower mantle and low viscosity upper mantle (Fig. 5b). The other is a five-layer model which splits the upper mantle into two layers (Figs 5a and c). The inversion yields a low viscosity asthenosphere immediately beneath the lithosphere. Compared to the four-layer model, the cost function of the best-fitting three-layer model is much larger (71.8 versus 83.2), while that of the five layer model is not obviously reduced (71.3 versus 71.8). This suggests that our inversion may be capable of resolving four layers while adding an additional layer beyond that does not reduce the cost function further. We also perform an additional inversion similar to those shown in Fig. 5(a) except that we move the depth of the viscosity jump from 660 to 1000 km. The best-fitting model yielded in the inversion has a cost function of 83.0, much larger than that shown in Fig. 5(a) (71.8). Thus we use the four-layer model with a viscosity jump across the 660 km discontinuity for the 3-D model inversions that follow.

We now invert for the fully 3-D viscosity. For this inversion, the oceanic lithosphere viscosity equals that of the pre-factor of the lithosphere layer (inverted values are shown in Fig. 5d), but the continental and weak plate margins (Fig. 3) are allowed to have different viscosities (Fig. 5e). The recovered radial viscosity is similar to the radial only model (Fig. 5d), but continental and oceanic lithospheres have different viscosities and plate boundaries are much weaker than plate interiors (Figs 5e and 6a), consistent with previous forward models (Zhong & Davies 1999; Tosi *et al.* 2009; Ghosh *et al.* 2010). Compared to the inverted model, increasing the viscosity of the Precambrian lithosphere slightly will increase the free-air gravity above upwellings (e.g. southern Africa) while decreasing the free-air gravity in subduction zones (e.g. East Asia). The inverted radially dependent viscosity is not significantly affected by including LVVs (compare Figs 5a with d), suggesting that the observational signals (gravitational fields and topography) at long wavelengths are controlled by the radial viscosity. There is a large scatter among the inferred LVVs parameters (Figs 5e and f). For example, all models with plate margins about one order less viscous than surrounding lithosphere fit the observations well

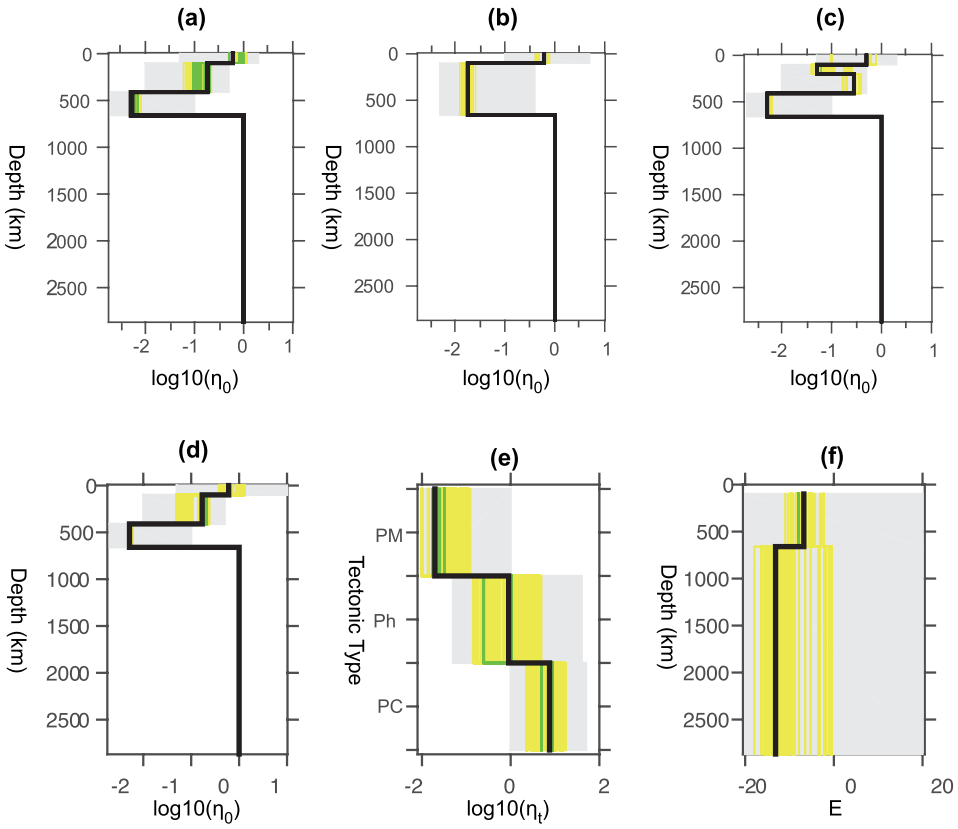

Figure 5. Recovered viscosity parameters. (a) Viscosity pre-factor of each layer for the four layer (lithosphere, upper mantle, transition zone and lower mantle) 1-D model. (b) Similar as (a), but combine the upper mantle and transition zone into one layer. (c) Similar as (a), but the upper mantle is split into two layers. (d) Viscosity pre-factor of each layer for the four layer 3-D model. (e) Viscosity jumps across each tectonic province. (f) The activation energy of each layer. We allow activation energy to be negative to account for possible balancing effects of other factors, which may overwhelm the effects of temperature on viscosity at long wavelengths. The meaning of symbols is the same as Fig. 4.

(Fig. 5e). However, we still find important attributes of lateral variations in viscosity. The viscosity of the pre-Cambrian lithosphere is about one order of magnitude higher than that of the oceanic and Phanerozoic lithosphere. Plate margins are weaker than plate interiors. The recovered non-dimensional activation energy in the mantle is close to zero.

The small (or even negative) activation energy found in the inversion is unexpected. We perform an extra 3-D inversion with the tectonic differences but the weak zones within the lithosphere removed to investigate the influence of the tectonic regionalization in the lithosphere on the activation energy. The derived apparent activation energies are also less than zero. This is consistent with Fig. 7, which demonstrates that the trade-offs between tectonic regionalization and activation energy are small. We perform a 3-D inversion constraining the activation energy to be no less than zero and find that that the recovered activation energy for the upper and lower mantle are both close to zero.

We analyse the sensitivity of the models (Fig. 6) and how the viscosity parameters trade off as they fit the observations (Fig. 7). Although the analysis indicates that all parameters affect the outcomes, the gravitational and topography fields are more sensitive to the radial viscosity than to LVVs. For example, the variation of upper-mantle activation energy has a smaller influence on the cost function than the upper-mantle viscosity pre-factor (Figs 6 and 7). The trend and trade-offs between inferred parameters are investigated with using a quadratic polynomial to fit the cost function at each computed point in the N-dimensional space. Although the quadratic polynomial is only an approximation of the actual, more complex cost function, it can reproduce the pattern and trend of the cost function (Figs 7a and b) without resampling the parameter space (Sambridge 1999). For example, we have evaluated the true cost function at evenly distributed grid points for the depth-dependent viscosity pre-factors (Fig. 7b). The trend predicted by our polynomial fitting is consistent with the true distribution. The trade-offs between viscosity parameters can be visualized through conditional distributions around the best-fitting model result (Fig. 7b). The viscosity pre-factors for the lithosphere and upper mantle strongly trade off with each other, noted earlier for radial dependent viscosity inversions (Thoraval & Richards 1997), with a negative slope such that a high viscosity lithosphere and low viscosity upper mantle fit the data as well as a model with a low viscosity lithosphere and high viscosity upper mantle. For example, the amplitude of dynamic topography low in Southeast Asia and dynamic topography high in the southwest Pacific (e.g. the Society Islands region) can be reduced by increasing the viscosity either in the lithosphere or upper mantle. On the other hand, the amplitude of dynamic topography low in Southeast Asia or dynamic topography high in the southwest Pacific can be increased by decreasing viscosity either in the lithosphere or upper mantle. The trade-offs between LVVs parameters are not prominent (Fig. 7). This may be related to the small sensitivity of the surface observations to these parameters (Fig. 7).

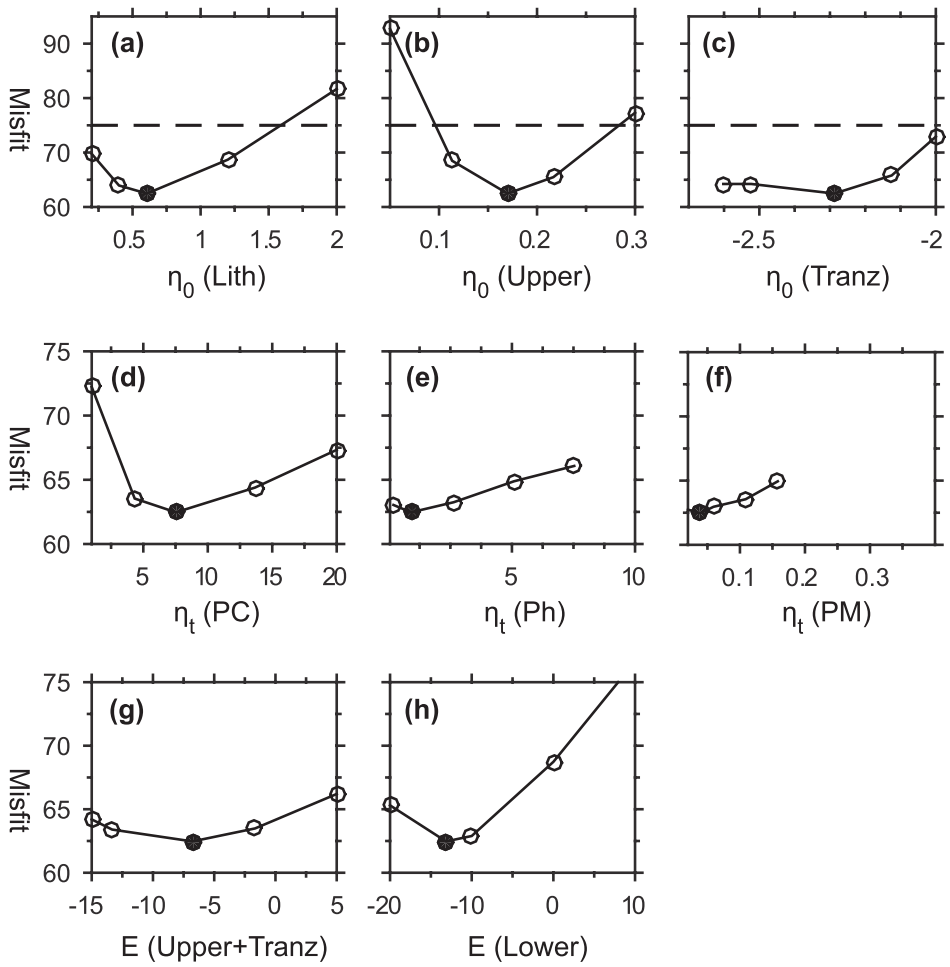

Figure 6. Sensitivity test for each parameter inverted, that is, fixing other parameters, investigate the cost function versus one parameter. The reference model (black solid circle) is our inverted mantle structure (black lines in Fig. 5). (a–c) Viscosity pre-factor for the oceanic lithosphere (0–100 km), upper mantle (100–410 km), transition zone (410–660 km) layers. (d–f) Viscosity contrast across the pre-Cambrian lithosphere, Phanerozoic lithosphere and plate margins. (g,h) Non-dimensional activation energy in the upper- and lower-mantle layers. Note that the Y-Axis limit for the uppermost panels is different from that in the middle and bottom panels.

3.2 Dynamic topography, free-air anomaly and GTR

The predicted and observed fields are generally consistent at long wavelengths (Figs 1 and 9). The Southeast Asia to Melanesia and South America subduction zones correspond to low dynamic topography but high geoids, positive free-air gravity anomaly, and positive vertical gravity gradients. The Pacific and African superswells correspond to high dynamic topography and high geoid, positive free-air gravity anomaly and positive vertical gravity gradient. Regions where slab remnants are thought to exist in the lower mantle (e.g. North and South America) forms a ring with low dynamic topography, low geoid, negative free-air gravity anomalies and negative vertical gravity gradient. Most continents lie above dynamic topography lows.

To further compare the observed residual topography and our predicted dynamic topography, we conduct spherical harmonic analysis for both the predicted dynamic topography (Fig. 8b) and the observed residual topography (Figs 8c and d). Although the dynamic topography has a number of localized high amplitude values (e.g. at the subduction zone where the predicted dynamic topography can reach −2 km, Fig. 8a), the amplitude of the long-wavelength (degree 2–3) components of the dynamic topography is ∼1 km (Fig. 8b). The long-wavelength components of the predicted dynamic topography are consistent with that of the observed residual topography in both amplitude and pattern (Figs 8b and c). For example, both the predicted and observed topographies yield ∼+500–700 m topography in southern Africa, ∼−1 km topography in East Asia and ∼+1 km topography in the south Pacific around the Society Islands. Compared to Fig. 8(c), which analyses 1006 high-accuracy residual topography observations from Hoggard *et al*. (2016), Fig. 8(d) includes ∼1000 extra observations, which have accurate sediment thickness measurements but the crustal thickness is not accurately known. The long-wavelength components from the leas-square analysis of these two different sets of point data are quite similar (Figs 8c and d).

We use a bootstrap method to estimate the highest spherical degrees that the ∼2100 residual topography points can be expanded to. We randomly choose 80 per cent per cent of the residual topography observations and compute the spherical harmonic fit. We repeat this process 30 times and then calculate the average fit error at the 80 per cent sampling points and 20 per cent per cent un-sampled points. When the maximum spherical harmonic expansion degree is larger than 5, the misfit at the 20 per cent un-sampled points is significantly larger than that at the 80 per cent sampling points. This bootstrap analysis suggests that the maximum degree to which the spherical harmonic expansion can be inferred is less than 5. We

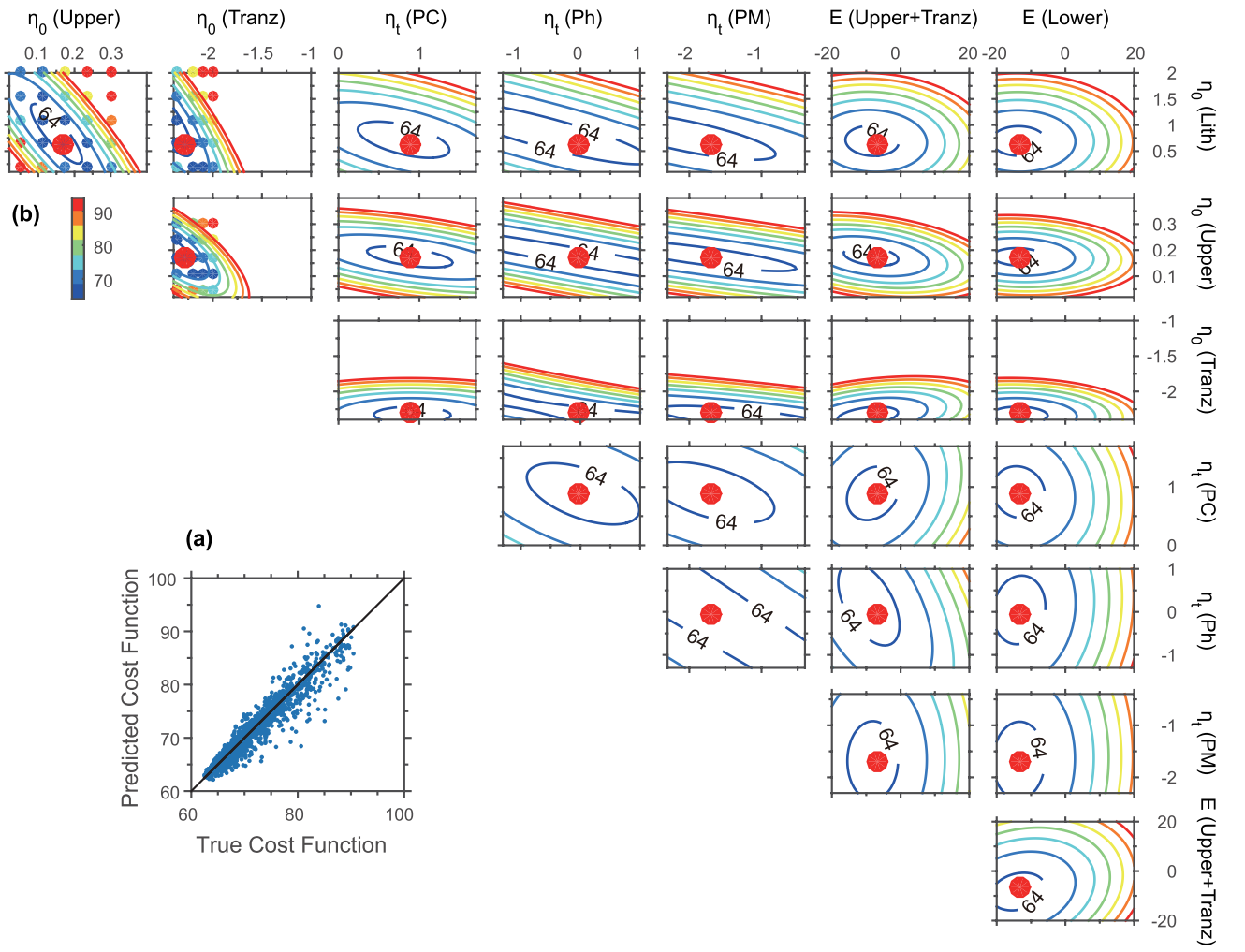

Figure 7. (a) A comparison between the real and the multiple variable quadratic polynomial fitting predicted cost function values at those points visited during the 3-D viscosity inversion. (b) Conditional distribution of the cost function. Fixing other six viscosity parameters at the inverted values, we plot the distribution of the cost function varying with the left two parameters. The inverted eight parameters include: pre-factor for the lithosphere, upper mantle and transition zone; viscosity contrast between the pre-Cambrian, Phanerozoic lithosphere, plate margins and the oceanic lithosphere; and activation of the upper- and lower-mantle layers. From top to bottom, each Y-axis represents the first seven parameters. From left to right, each X-axis represents the last seven parameters. Large red dots represent the inverted viscosity parameters. The real cost function values based on the grid-search (small dots in the upper-left panels) and that predicted by multivariable quadratic polynomial fitting (contour lines) are consistent.

compare the power spectra for the dynamic and residual topographies at the ∼2100 residual topography observation points. The power of the long-wavelength residual and dynamic topographies are comparable (Fig. 9). However, the predicted dynamic topography peaks at degree 2 while the residual topography spectra are more flat.

Although the predicted dynamic topography reproduces the observed residual topography at long wavelengths, it does not reproduce the short wavelength variations of residual topography. For example, although offshore Argentina and offshore Chile are only a few hundred kilometres away, residual topography decreases from ∼+500 m offshore Chile to ∼−1000 m within the Argentine Basin. In contrast, the predicted dynamic topography demonstrates only a gradual decrease from offshore Chile to the Argentine Basin.

Our results indicate that the fit to the free-air gravity does not preclude the presence of a ∼1 km amplitude dynamic topography at long wavelengths (Figs 1 and 9a). For example, in Southeast Asia, dynamic topography reaches ∼−1000 m while in Pacific superswells, the dynamic topography reaches ∼+1000 m. To investigate the relationship between gravity anomaly and dynamic topography, we estimate the GTR and the correlation between predicted free-air anomaly and dynamic topography at randomly distributed points across the globe that sample the field at different wavelengths (Fig. 10).

For the longest wavelengths (degree 2–3, Fig. 10a), although dynamic topography and free-air anomaly show some correlations regionally, they are poorly correlated globally and the GTR is small (0.8 mGal km^{-1}). For example, offshore Western Australia dynamic topography and free-air anomaly demonstrate a clear negative correlation with lower dynamic topography corresponding to a higher gravity anomaly. On the other hand, at Wilkes Land margin of Antarctic (south of Australia), dynamic topography and gravity anomaly have a positive correlation. However, dynamic topography and free-air anomaly are not correlated globally. This is because at the longest wavelengths, free-air anomaly is sensitive to mantle density heterogeneity within the whole mantle and the gravity

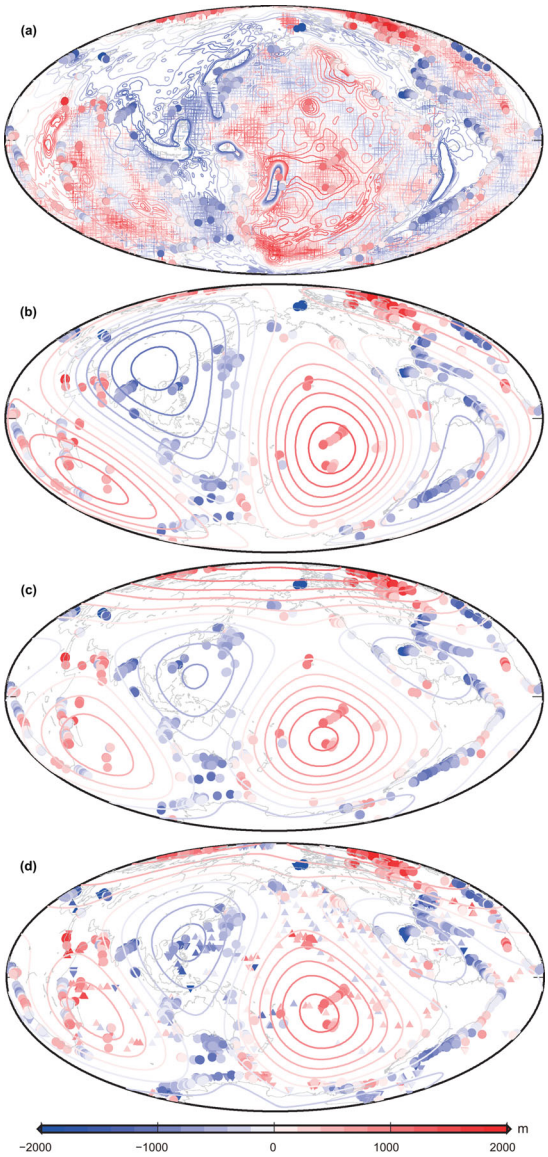

Figure 8. Comparison of inverted dynamic topography with observed residual topography. (a) Observed residual topography superimposed on the predicted dynamic topography at a contour interval of 200 m. (b) Long-wavelength component (degree 0–3) of the predicted dynamic topography with 1006 high-accuracy residual topography observations (Hoggard *et al*. 2016) superimposed. (c) Long-wavelength components (degree 0–3) from the least squares analysis of 1006 high accurate residual topography observations (Hoggard *et al*. 2016). (d) Long-wavelength components (degree 0–3) of observed 2120 residual topography observations (1006 high accurate residual topography and 1114 extra observations with crustal thickness unmeasured; Hoggard *et al*. 2016). In (a), crosses represent residual topography following the procedure in Winterbourne *et al*. (2014) from ship-track bathymetry (assembled digitally by Smith & Sandwell 1997) with the isostatic effect of sediment loading and lithosphere thermal cooling removed. Sediment thickness data are based on the NGDC grid (Whittaker *et al*. 2013) and oceanic plate age map is from Müller *et al*. (2008) with the reference depth-age curve of Crosby & McKenzie (2009). Areas of known oceanic plateau are excised and the resulting residual topography along ship-tracks is interpolated onto evenly distributed $2^\circ \times 2^\circ$ grids. Solid circles represent 1006 high accuracy residual topography observations from Hoggard *et al*. (2016), in which sedimentary and crustal thicknesses are known with high accuracy. Upward pointing triangles represent 488 points, which give the lower limit for residual depth; downward pointing triangles represent 626 points, which give the upper limit for residual depth. Contours are for inverted dynamic topography with a 200 m interval.

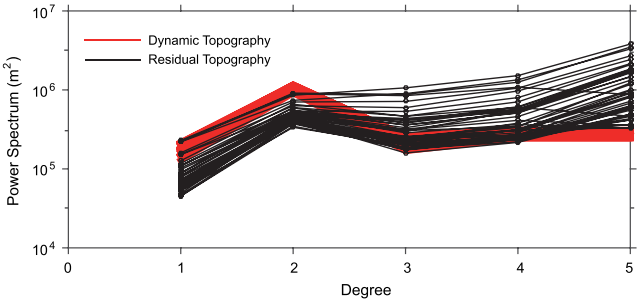

Figure 9. Power spectra of the spherical harmonic analysis of the residual topography point measurements and dynamic topography that is required to fit the components of the gravity fields through the dynamic flow model. The bounds of the power spectra of the predicted dynamic topography (red band) are based on the 10 per cent best-fitting models. Each of the fifty estimations of the residual topography power spectra with 80 per cent randomly sampled points is represented by a black line.

kernels change sign with depth (Hager 1984; Hager & Richards 1989; Simmons *et al*. 2010).

Between degrees 4–10 (Fig. 10b), the correlation between dynamic topography and free-air anomaly is high but the GTR is negative (-14.7 mGal km^{-1}), suggesting that positive dynamic topography corresponds to negative gravity anomaly and negative dynamic topography corresponds to positive gravity anomaly. In the model, the gravity anomaly at degree 4–10 is mainly controlled by subducted slabs in the mid-mantle (Hager 1984; Hager & Richards 1989) in which the free-air anomaly kernel is positive while the dynamic topography kernel is negative (Hager 1984; Hager & Richards 1989). With the recovered viscosity jump across the 660 km discontinuity (Hager & Richards 1989), amplitudes of positive (negative) surface dynamic topography induced by subducted slabs (or upwelling flow) are significantly reduced compared with those obtained in a uniform viscosity mantle (Hager & Richards 1989). An example of positive residual topography, but negative gravity anomaly is the pattern found in the Ross Sea region (Figs 1 and 8a), as previously documented (Spasojevic *et al*. 2010; Sutherland *et al*. 2010). An example of the negative topography and positive gravity anomaly is western Pacific subduction zones, especially evident through -1 km residual topography over the entire Philippine Sea plate (Fig. 8a; Winterbourne *et al*. 2014) but within a region of high gravity (Fig. 1).

At shorter wavelengths (e.g. between degree 15–20, Fig. 10c), the correlation between dynamic topography and free-air anomaly is high and GTR is positive (31.2 mGal km^{-1}). The gravity and dynamic topography kernels in the lower mantle are close to zero for wavelengths shorter than $\sim$5000 km, suggesting that buoyancy heterogeneities in the lower mantle do not affect short wavelength gravity and dynamic topography. Both free-air and dynamic topography kernels are negative over these wavelengths, yielding a positive correlation between dynamic topography and free-air anomaly. Iceland (and some other hotspots), which has both high dynamic topography and free-air gravity anomaly is an example. Notice that the amplitudes of dynamic topography ($\sim\pm$500 m, Fig. 10c) within this range of wavelengths is much smaller than that at longer wavelengths ($\sim\pm$1000 m, Figs 10a and b).

Dynamic topography is mainly induced by vertical stresses imposed on the lithosphere by mantle flow. The large-scale plate interior tectonic regime (compression, extension, strike-slip or neutral), on the other hand, is affected by the mantle flow induced

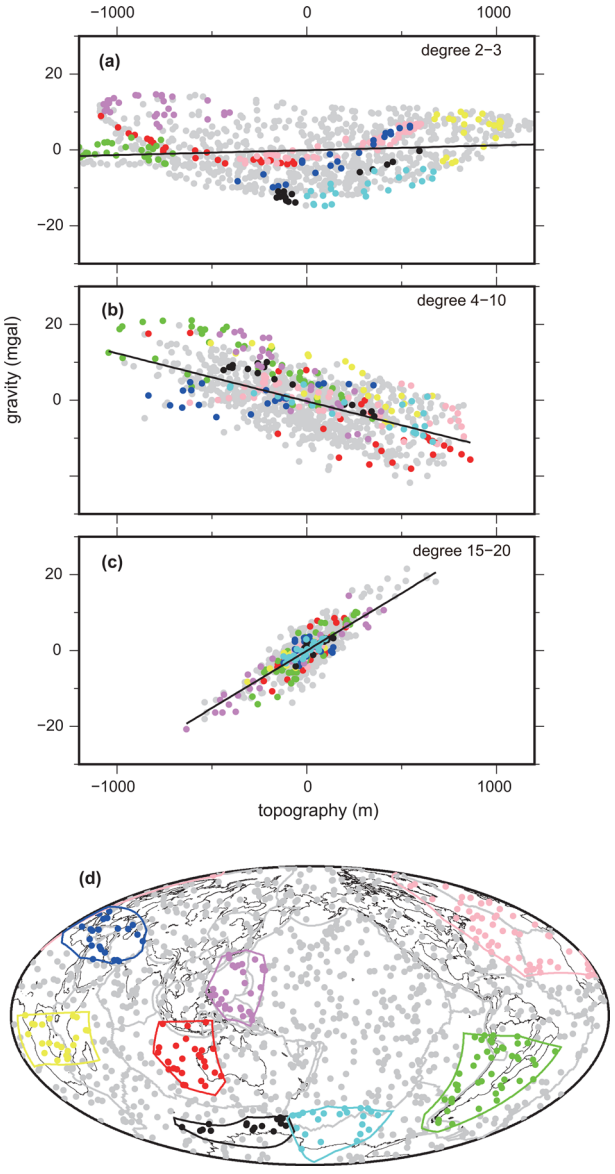

Figure 10. Relationships between predicted dynamic topography and free-air gravity anomaly at randomly chosen points. (a) At spherical harmonic degrees 2–3, (b) at spherical harmonic degree 4–10 and (c) at spherical harmonic degrees 15–20. (d) Location of sample points. Points inside six regions are colour-coded while those outside these regions are plotted in grey.

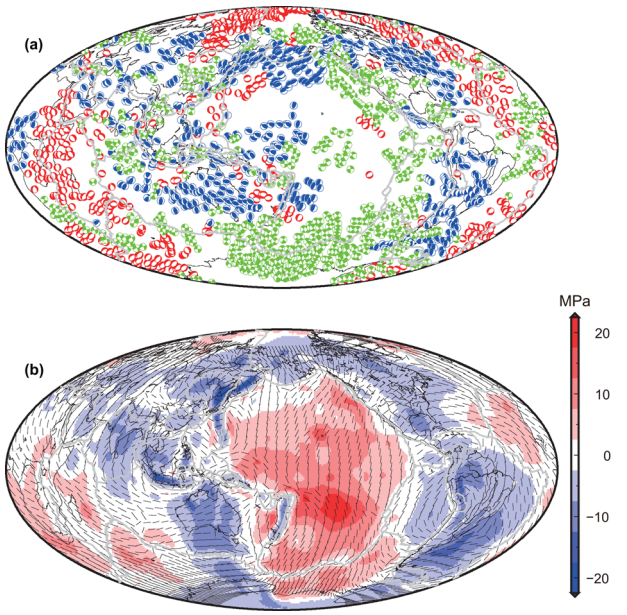

Figure 11. Comparison between observed (a) and predicted, mantle flow induced (b) lithospheric stress regime. In (a), observed stress data are plotted with implied focal mechanisms (lower-hemisphere stereographic projection). Blue, red and green represent thrust, normal and strike-slip stress regimes, respectively. In (b), horizontal stress direction and magnitude are represented by black bar and colour, respectively. Positive and negative values represent extension and compression respectively.

horizontal stresses. Based on Anderson's theory of faulting, positive and negative values of the average amplitude of the horizontal stress correspond to normal and thrust faulting, respectively (Turcotte & Schubert 2014). We compare mantle flow induced lithospheric horizontal stress magnitude (Fig. 11) with the observed stress regime (Koptev *et al*. 2013), which is a regional average of the World Stress Map data (Heidbach *et al*. 2010). Although the lithospheric stress field is affected by multiple factors, including mantle flow, plate boundary forces and topographic potentials (Zoback 1992), the predicted stress amplitude is generally consistent with previous calculations (Lithgow-Bertelloni & Guynn 2004; Ghosh *et al*. 2013) and the observed stress regimes. For example, predicted extension (the average horizontal lithospheric stress is positive) in east and southern Africa, central and north Atlantic and compression (the average horizontal lithospheric stress is negative) in Southeast Asia, South America, and eastern North America is consistent with the observations. This consistency between predicted stress magnitude and observed stress regimes provides circumstantial support for the predicted dynamic topography.

4 DISCUSSION AND CONCLUSION

Knowledge of mantle viscosity is key for our understanding of earth evolution and dynamics. However, the inversion of mantle viscosity has been a long-standing problem, especially since there have been only a few attempts to recover the lateral variations in viscosity (Čadek & Fleitout 2003, 2006; Ghosh *et al*. 2010, 2013). We update Powell's method, which enables us to invert for model parameters efficiently. Then we explicitly invert for mantle viscosity, including depth- and temperature- dependent and tectonically regionalized viscosity and investigate the trade-offs between different viscosity parameters.

Our results suggest that, compared to radial viscosity variations, LVVs have less influence on long-wavelength observations. This result is consistent with previous forward studies (Richards & Hager 1989; King & Hager 1994; Moucha *et al*. 2007; Ghosh *et al*. 2010). Previous studies also suggest that LVVs do not strongly affect the lithospheric stress field (Conrad and Lithgow-Bertelloni 2006; Naliboff *et al*. 2009). However, considering LVVs in the mantle may still improve the fit to surface observations (Zhong & Davies 1999; Ghosh *et al*. 2010) and LVVs may be recovered through inversion, although with large uncertainty (Fig. 4).

The recovered apparent activation energy, which is close to zero or even negative (Fig. 5), suggests that temperature heterogeneity induced LVVs are small or balanced by other factors at long wavelengths, with the slab region no more than ∼one order of magnitude higher in viscosity than the surrounding mantle at long wavelengths.

This result is consistent with previous forward studies (Moresi & Gurnis 1996; Zhong & Davies 1999; Yoshida & Nakakuki 2009). This inverted small activation energy might be one of the reasons why the pure slab subduction induced mantle density model can reproduce the observed geoid for radially layered viscosity (Ricard *et al*. 1993) but fail to reproduce the observed geoid when temperature dependent viscosity is considered (Zhong & Davies 1999).

There are likely two reasons for the recovery of lateral variations in viscosity, which are much smaller than those variations predicted by forward models using laboratory-based constitutive relations in which the variations are suggested to be at least several orders of magnitude (Stadler *et al*. 2010; Alisic *et al*. 2012): either the lateral variations are small at long wavelengths or at long wavelengths large LVVs are being averaged out. In the first case, there could be several factors lowering LVVs compared to those predictions from purely temperature, such as ionic diffusion (Ammann *et al*. 2010), grain size (Glišović *et al*. 2015) and stress and yielding induced weakening (Hines & Billen 2012; Jadamec 2015). When yielding and dislocation creep regimes are considered, some part of the slab might be weakened. Although most parts of the slab are still strong, they are weakly connected to the surface, yielding dynamic topography and gravitational fields similar to that of a homogeneous weak slab (Hines & Billen 2012). Considering lateral grain size variations may further reduce the LVVs (Glišović *et al*. 2015). Phase transformation from the orthorhombic to the tetragonal structure perovskite and grain size reduction when the cold slab passes through the 660 km discontinuity may also contribute to the low apparent activation energy in the lower mantle (Karato & Li 1992; Solomatov 1996). In the second case, subduction of the high viscosity slab into the mantle may weaken the surrounding mantle. Under the dislocation creep regime (which might operate within regions close to slabs both in the upper and lower mantle; McNamara *et al*. 2002), subduction of a high viscosity slab produces a zone of weakening surrounding the slab (Stadler *et al*. 2010; Jadamec 2015). Dehydration of the subducted slab can also weaken the overriding mantle (Hebert *et al*. 2009), forming low-viscosity channel or mantle wedge which arguably strongly affects slab dynamics (Billen & Gurnis 2001; Manea & Gurnis 2007). This short wavelength LVVs with high viscosity slabs and low viscosity surrounding mantle may be smoothed out for long wavelengths (larger than ∼5000 km) during inversion. However, we suggest that although LVVs over long wavelengths may not be significant, it may be large at short wavelengths, which is putatively a critical factor governing plate motions (Stadler *et al*. 2010). Our inversion results highlight the necessity of investigating detailed subduction zone viscosity structures.

Our inversions suggest that the subduction zones have a lower viscosity than the less deformed surrounding mantle at large scale. This is consistent with previous laboratory experiments (Girard *et al*. 2016) suggesting that strain weakening and shear localization likely occur in the lower mantle. The inverted mantle viscosity structures have significant implications on the studies of thermochemical evolutions of the mantle. For example, previous studies (Solomatov & Reese 2008; Yang & Fu 2014) suggest that the dynamics of the thermochemical piles in the lower mantle may be significantly different from those assuming pure temperature-dependent viscosity.

Rheology and strength of the continental lithosphere remain contentious. Many studies suggest that the continental lithosphere has higher effective strength due to its low temperature, water deficiency (Peslier *et al*. 2010) and survival since the Archean (Jordan 1978). However, the Phanerozoic lithosphere might be weaker in light of its extensive deformation. The inversions suggest that the pre-Cambrian lithosphere is ∼one order of magnitude higher in viscosity compared to both oceanic and Phanerozoic lithosphere, while the oceanic and Phanerozoic lithosphere have similar viscosities. Plate margin has long been suggested to have low viscosity (Gurnis *et al*. 2000b), due to yielding, strain weakening and partial melting (Bercovici 2003). The inversions are consistent with these suggestions. Previous forward calculations indicate that the weak plate boundaries help to reproduce observed plate motion and yields better geoid models (Zhong & Davies 1999; Tosi *et al*. 2009; Ghosh *et al*. 2010).

Table 3. Inverted ratios between non-dim temperature and shear wave velocity perturbation. Scaling ratios of positive and negative velocity perturbations are allowed to be different.

Depth (km)	dT/dV_s (positive, unit 1E-4)	dT/dV_s (negative, unit 1E-4)
250–410	1.43	2
410–660	1.0	6.0
660–1700	3.0	4.8
1700–2867	8	8

Consistent with previous inversions (Hager & Richards 1989; King 1995; Panasyuk & Hager 2000a; Mitrovica & Forte 2004; Soldati *et al*. 2009), we assume that the viscosity boundary coincides with the 660 km phase boundary. However, Rudolph *et al*. (2015) has recently argued that viscosity increases at ∼1000 km instead of at 660 km depth. We performed an additional inversion similar to those shown (Fig. 5a) except that we move the 660 km viscosity boundary to 1000 km depth. The best-fitting model yielded in the inversion has a larger cost function than that shown in Fig. 5(a). Movement of an internal viscosity jump from 660 to 1000 km might be problematic in fits to the stress patterns inferred from deep focus earthquakes which show that slabs descending down to only the upper mantle are in downdip tension while those extending to the transition zone are in downdip compression (Isacks & Molnar 1971). Generic flow models (Vassiliou *et al*. 1984; Alpert *et al*. 2010) and models tailored to observed structure and seismicity (Billen *et al*. 2003; Alisic *et al*. 2010) requires either a jump in viscosity at 660 km or an increasing gradient between 410 and 660 km.

The inverted upper mantle has a larger effective viscosity than the transition zone, found previously (King 1995; Soldati *et al*. 2009), usually interpreted as indicative of mantle hydration in the transition zone (Pearson *et al*. 2014). Uncertainties of the seismic tomographic models would be expected to influence the parameters recovered in inversions (Lee *et al*. 2011). However, all the seismic tomography models tested by Lee *et al*. (2011) yield a low viscosity transition zone compared to the upper mantle. The five layer viscosity inversions yield a low viscosity asthenosphere (Fig. 5c). However, compared to the four layer viscosity inversions (Fig. 5a), the best-fitting cost function is not significantly reduced. This suggests that the surface observations invoked here are not sensitive to the asthenosphere viscosity or that the asthenosphere viscosity trades off with the lithosphere and upper-mantle viscosities (Thoraval & Richards 1997). Other observations, for example, plate motion, may be more sensitive to asthenosphere viscosity. However, much higher resolution mesh is clearly needed to model plate motion properly (Stadler *et al*. 2010).

Although we focus on inversion of viscosity parameters, we also attempted to recover the mantle density structure after deriving the best-fitting viscosity structure (Table 2). The recovered dT/dV_s for each layer are listed in Table 3. The recovered dT/dV_s in the upper mantle are much smaller than those in the lower mantle, consistent

with previous studies (Deschamps *et al*. 2001) and suggests that relationship between seismic velocity anomaly and density is complex in the upper mantle (Deschamps *et al*. 2001). Our inverted dT/dV_s ratios in the lower mantle are consistent with previous studies (e.g. Karato & Karki 2001) and the yielded lateral density variations, with amplitude generally less than ∼30 kg m^{-3} (Fig. 3c), are also consistent with previous studies (Gurnis *et al*. 2000a; Simmons *et al*. 2010).

Although the concept that mantle convection imposes normal stress on the lithosphere and produces dynamic topography is widely accepted, little consensus has been reached on the amplitude of dynamic topography. Our model, which fits the long-wavelength geoid, free-air anomaly and gravity gradients, predicts large amplitude, ∼1 km, long-wavelength dynamic topography, consistent with the long-wavelength components of the recently compiled high accuracy residual topography. This suggests that the observed free-air gravity anomaly does not require small amplitude of dynamic topography, in contrast to the conclusion of Molnar *et al*. (2015). The inconsistency between the model here and that of Molnar *et al*. (2015) arises from GTR that depends on wavelengths (spherical harmonic degree) for a viscously heterogeneous mantle (Moresi & Parsons 1995) which is overlooked by Molnar *et al*. (2015). At wavelength longer than ∼5000 km, the amplitude of dynamic topography is large, while the amplitude of free-air anomaly is small (Fig. 7). This is because that at the longest wavelength GTR is close to zero (degree 2–3) or negative (degree 4–12). Previous studies in 2-D Cartesian domain (McKenzie 1994; Moresi & Parsons 1995) also suggests that GTR varies with wavelength.

Contrary to Hoggard *et al*. (2016), who argue that the amplitude of the long-wavelength dynamic topography is no larger than 500 m, our analysis of the observed residual topography demonstrates a ∼1000 m amplitude at long-wavelength (Fig. 8), consistent with the predicted dynamic topography. One reason for the small amplitude derived by Hoggard *et al*. (2016) is their use of a 'model' of dynamic topography within continents. Hoggard *et al*. (2016) use a model with a constant 50 mgal km^{-1} admittance to transform free-air gravity to residual topography for onshore regions. However, the admittance is expected to vary with wavelength and location with negative admittance at wavelengths of ∼5000 to ∼10 000 km (Fig. 8). This transformation predicts ∼+1 km high residual topography onshore Southeast Asia. However, their accurate point measurements of the residual topography suggest ∼−1 km low residual topography in this region. Consequently, summing their model of positive dynamic topography within Southeast Asia and over northern Australia with the observed negative, off shore residual topography, effectively annihilates the long wavelengths over Southeast Asia in the model of Hoggard *et al*. (2016). In addition, because the sediment and crustal thicknesses are not accurately known, residual topography based on ship-tracks may also have large uncertainties.

We analyse the high-accuracy point measurements of residual topography compiled by Hoggard *et al*. (2016). The patterns and amplitude of the long-wavelength components of residual topography (Figs 8c and d) are very close to those of our predicted dynamic topography (Fig. 8b). For example, both the long-wavelength residual and dynamic topography yield ∼+500–700 m topography in southern Africa, ∼−1 km in east Eurasia and ∼+1 km topography in southern Pacific around the Society Islands. The long-wavelength residual topography and dynamic topography are broadly consistent. However, significant differences still exist between them. For example, the degree 2 peak in dynamic topography is not observed in the residual topography. Our model predicts ∼−500 m dynamic topography across South America which is not shown in the long-wavelength residual topography. Considering that our predicted lithospheric stress regime is consistent with the observed stress regime in this region (Fig. 11), we suggest that our predicted negative dynamic topography across South America is reasonable. More work related to both residual topography measurements and mantle dynamics models is needed to reconcile this difference.

Although some residual topography observations (Czarnota *et al*. 2013; Winterbourne *et al*. 2014; Hoggard *et al*. 2016) have accurate sedimentary and crustal thicknesses corrections, they are sparse and located primarily on oceanic lithosphere adjacent to continental margins, leaving residual topography within most part of the oceanic lithosphere unconstrained. The choice of the reference age-depth relationship also strongly influences the determined residual topography. Following the procedure of Winterbourne *et al*. (2014), we determine residual topography from ship-track bathymetry (assembled digitally by Smith & Sandwell 1997), which covers large parts of oceanic crust (Fig. 8). Avoiding areas of thick sediments and oceanic plateaus, the isostatic loading of sediment and thermal cooling of the lithosphere are removed from the observed bathymetry. The derived residual topography corroborates high long-wavelength topography in the southwest Pacific and around southern Africa, consistent with our predicted dynamic topography (Fig. 8). The most significant difference between residual topography and dynamic topography lies in the northwest Pacific, where the residual topography is ∼−500 m while the dynamic topography is ∼+500 m. Previous inversions suggest that substituting the S40RTS tomography model with SAW642ANb cannot reproduce the low residual topography in northwest Pacific (fig. 7 in Liu & Zhong 2016). One possibility for the low residual topography but moderate high dynamic topography within northwest Pacific are shallow seismic velocity (and hence density) heterogeneities that are yet to be accounted for. We added the ship-track based residual topography into a separate inversion to assess its influence on recovered parameters. The new inversions yield similar viscosity structure as that in Fig. 5. We have also changed the reference age-depth relationship from that of Crosby & McKenzie (2009) to the half-space cooling model and recalculated the residual topography. Compared to that with the Crosby age-depth relationship as a reference, the new calculated residual topography based on the half-space cooling model predicts higher positive residual topography and shallower negative residual topography in the old oceanic basins. However, the inverted mantle viscosity structure is not significantly influenced by the choice of the reference age-depth relationship.

There remain factors that may affect the inversion of mantle viscosity structure and the prediction of dynamic topography which are yet to be fully accounted for. For example, the model parameterization, including the number and depth of layers (Rudolph *et al*. 2015), or the smoothness of the viscosity (Constable *et al*. 1987) may affect the inversion. Possible composition heterogeneity in the mantle (Ballmer *et al*. 2015; Liu & Zhong 2015) may also affect the inversion. Also, due to the limitation of tomography models and the simplified mantle viscosity and temperature structure, shorter wavelength features evident in residual topography are poorly reproduced by dynamic topography. Self-consistent velocity-temperature and velocity-density scalings (Stixrude & Lithgow-Bertelloni 2007) with higher-resolution tomography models should also be considered in the future. In summary, based on the present results, we conclude that: (1) Geodynamic observations are mainly controlled by the radial variations in viscosity, but are also influenced by LVVs. (2) LVVs due to temperature might be balanced by other processes. (3) Plate margins are much weaker than plate interiors. The

pre-Cambrian lithosphere has ∼one order higher viscosity than the Oceanic and Phanerozoic lithosphere. (4) Both the compiled high-accuracy residual topography and modelled dynamic topography yield ∼1 km amplitude at long wavelengths suggesting that the observed free-air gravity anomaly does not preclude the existence of long-wavelength dynamic topography, which can reach ∼1 km in amplitude.

ACKNOWLEDGEMENTS

This work was supported by Statoil ASA and the National Science Foundation (under awards EAR 10-28978, EAR-1247022 and EAR-1358646). The authors thank Thorsten Becker and Carolina Lithgow-Bertelloni for their helpful comments.

REFERENCES

Alisic, L., Gurnis, M., Stadler, G., Burstedde, C., Wilcox, L.C. & Ghattas, O., 2010. Slab stress and strain rate as constraints on global mantle flow, *Geophys. Res. Lett.,* **37,** L22308, doi:10.1029/2010GL045312.

Alisic, L., Gurnis, M., Stadler, G., Burstedde, C. & Ghattas, O., 2012. Multi-scale dynamics and rheology of mantle flow with plates, *J. geophys. Res.,* **117,** B10402, doi:10.1029/2012JB009234.

Alpert, L., Becker, T. & Bailey, I., 2010. Global slab deformation and centroid moment tensor constraints on viscosity, *Geochem. Geophys. Geosyst.,* **11,** doi:10.1029/2010GC003301.

Ammann, M., Brodholt, J., Wookey, J. & Dobson, D., 2010. First-principles constraints on diffusion in lower-mantle minerals and a weak D" layer, *Nature,* **465,** 462–465.

Ballmer, M.D., Schmerr, N.C., Nakagawa, T. & Ritsema, J., 2015. Compositional mantle layering revealed by slab stagnation at ∼1000-km depth, *Sci. Adv.,* **1,** e1500815.

Becker, T.W., Faccenna, C., Humphreys, E.D., Lowry, A.R. & Miller, M.S., 2014. Static and dynamic support of western United States topography, *Earth planet. Sci. Lett.,* **402,** 234–246.

Bercovici, D., 2003. The generation of plate tectonics from mantle convection, *Earth planet. Sci. Lett.,* **205,** 107–121.

Billen, M.I. & Gurnis, M., 2001. A low viscosity wedge in subduction zones, *Earth planet. Sci. Lett.,* **193,** 227–236.

Billen, M.I., Gurnis, M. & Simons, M., 2003. Multiscale dynamics of the Tonga—Kermadec subduction zone, *Geophys. J. Int.,* **153,** 359–388.

Čadek, O. & Fleitout, L., 2003. Effect of lateral viscosity variations in the top 300 km on the geoid and dynamic topography, *Geophys. J. Int.,* **152,** 566–580.

Čadek, O. & Fleitout, L., 2006. Effect of lateral viscosity variations in the core-mantle boundary region on predictions of the long-wavelength geoid, *Stud. Geophys. Geod.,* **50,** 217–232.

Chambat, F., Ricard, Y. & Valette, B., 2010. Flattening of the Earth: further from hydrostaticity than previously estimated, *Geophys. J. Int.,* **183,** 727–732.

Chase, C.G., 1979. Subduction, the geoid, and lower mantle convection, *Nature,* **282,** 464–468.

Colli, L., Ghelichkhan, S. & Bunge, H.P., 2016. On the ratio of dynamic topography and gravity anomalies in a dynamic Earth, *Geophys. Res. Lett.,* **43,** doi:10.1002/2016GL067929.

Conrad, C.P. & Husson, L., 2009. Influence of dynamic topography on sea level and its rate of change, *Lithosphere,* **1,** 110–120.

Conrad, C.P. & Lithgow-Bertelloni, C., 2006. Influence of continental roots and asthenosphere on plate-mantle coupling, *Geophys. Res. Lett.,* **33,** doi:10.1029/2005GL025621.

Constable, S.C., Parker, R.L. & Constable, C.G., 1987. Occam's inversion: a practical algorithm for generating smooth models from electromagnetic sounding data, *Geophysics,* **52,** 289–300.

Crosby, A. & McKenzie, D., 2009. An analysis of young ocean depth, gravity and global residual topography, *Geophys. J. Int.,* **178,** 1198–1219.

Crosby, A., McKenzie, D. & Sclater, J., 2006. The relationship between depth, age and gravity in the oceans, *Geophys. J. Int.,* **166,** 553–573.

Crough, S.T., 1978. Thermal origin of mid-plate hot-spot swells, *Geophys. J. Int.,* **55,** 451–469.

Czarnota, K., Hoggard, M., White, N. & Winterbourne, J., 2013. Spatial and temporal patterns of Cenozoic dynamic topography around Australia, *Geochem. Geophys. Geosyst.*, **14,** 634–658.

Davies, G.F. & Pribac, F., 1993. Mesozoic seafloor subsidence and the Darwin Rise, past and present, in *The Mesozoic Pacific: Geology, Tectonics, and Volcanism*, pp. 39–52, eds Pringle, M.S., Sager, W.W., Sliter, W.V. & Stein, S., doi:10.1029/GM1077p0039.

Deschamps, F., Snieder, R. & Trampert, J., 2001. The relative density-to-shear velocity scaling in the uppermost mantle, *Phys. Earth planet. Inter.,* **124,** 193–212.

Djomani, Y.H.P., O'Reilly, S.Y., Griffin, W. & Morgan, P., 2001. The density structure of subcontinental lithosphere through time, *Earth planet. Sci. Lett.,* **184,** 605–621.

Faccenna, C., Becker, T.W., Miller, M.S., Serpelloni, E. & Willett, S.D., 2014. Isostasy, dynamic topography, and the elevation of the Apennines of Italy, *Earth planet. Sci. Lett.,* **407,** 163–174.

Flament, N., 2014. Linking plate tectonics and mantle flow to Earth's topography, *Geology,* **42,** 927–928.

Flament, N., Gurnis, M. & Müller, R.D., 2013. A review of observations and models of dynamic topography, *Lithosphere,* **5,** 189–210.

Geruo, A., Wahr, J. & Zhong, S., 2013. Computations of the viscoelastic response of a 3-D compressible Earth to surface loading: an application to Glacial Isostatic Adjustment in Antarctica and Canada, *Geophys. J. Int.,* **192,** 557–572.

Ghosh, A., Becker, T. & Zhong, S., 2010. Effects of lateral viscosity variations on the geoid, *Geophys. Res. Lett.,* **37,** doi:10.1029/2009GL040426.

Ghosh, A., Becker, T.W. & Humphreys, E.D., 2013. Dynamics of the North American continent, *Geophys. J. Int.,* **194**(2), 651–669.

Girard, J., Amulele, G., Farla, R., Mohiuddin, A. & Karato, S.-i., 2016. Shear deformation of bridgmanite and magnesiowüstite aggregates at lower mantle conditions, *Science,* **351,** 144–147.

Glišović, P., Forte, A.M. & Ammann, M.W., 2015. Variations in grain size and viscosity based on vacancy diffusion in minerals, seismic tomography, and geodynamically inferred mantle rheology, *Geophys. Res. Lett.,* **42,** 6278–6286.

Greff-Lefftz, M., Métivier, L., Panet, I., Caron, L., Pajot-Métivier, G. & Bouman, J., 2016. Joint analysis of GOCE gravity gradients data of gravitational potential and of gravity with seismological and geodynamic observations to infer mantle properties, *Geophys. J. Int.,* **205,** 257–283.

Gudmundsson, Ó. & Sambridge, M., 1998. A regionalized upper mantle (RUM) seismic model, *J. geophys. Res.,* **103,** 7121–7136.

Gurnis, M., 1990. Ridge spreading, subduction, and sea level fluctuations, *Science,* **250,** 970–972.

Gurnis, M., Mitrovica, J.X., Ritsema, J. & van Heijst, H.J., 2000a. Constraining mantle density structure using geological evidence of surface uplift rates: the case of the African superplume, *Geochem. Geophys. Geosyst.,* **1,** doi:10.1029/1999GC000035.

Gurnis, M., Zhong, S. & Toth, J., 2000b. On the competing roles of fault reactivation and brittle failure in generating plate tectonics from mantle convection, in *The History and Dynamics of Global Plate Motions*, pp. 73–94, doi:10.1029/GM1121p0073.

Hager, B. & Richards, M., 1989. Long-wavelength variations in Earth's geoid: physical models and dynamical implications, *Phil. Trans. R. Soc. Lond., A,* **328,** 309–327.

Hager, B.H., 1984. Subducted slabs and the geoid: constraints on mantle rheology and flow, *J. geophys. Res.,* **89,** 6003–6015.

Hager, B.H., Clayton, R.W., Richards, M.A., Comer, R.P. & Dziewonski, A.M., 1985. Lower mantle heterogeneity, dynamic topography and the geoid, *Nature,* **313,** 541–545.

Hebert, L.B., Antoshechkina, P., Asimow, P. & Gurnis, M., 2009. Emergence of a low-viscosity channel in subduction zones through the coupling of mantle flow and thermodynamics, *Earth planet. Sci. Lett.,* **278,** 243–256.

Heidbach, O., Tingay, M., Barth, A., Reinecker, J., Kurfeß, D. & Müller, B., 2010. Global crustal stress pattern based on the World Stress Map database release 2008, *Tectonophysics,* **482,** 3–15.

Hines, J.M. & Billen, M.I., 2012. Sensitivity of the short-to intermediate-wavelength geoid to rheologic structure in subduction zones, *J. geophys. Res.,* **117,** doi:10.1029/2011JB008978.

Hoggard, M., White, N. & Al-Attar, D., 2016. Global dynamic topography observations reveal limited influence of large-scale mantle flow, *Nat. Geosci.,* **9**(6), doi:10.1038/NGEO2709.

Husson, L., Guillaume, B., Funiciello, F., Faccenna, C. & Royden, L.H., 2012. Unraveling topography around subduction zones from laboratory models, *Tectonophysics,* **526,** 5–15.

Isacks, B. & Molnar, P., 1971. Distribution of stresses in the descending lithosphere from a global survey of focal-mechanism solutions of mantle earthquakes, *Rev. Geophys.,* **9,** 103–174.

Jadamec, M., 2015. Slab-driven mantle weakening and rapid mantle flow, in *Subduction Dynamics: From Mantle Flow to Mega Disasters*, pp. 135–155, eds Morra, G., Yuen, D.A., King, S.D., Lee, S.-M. & Stein, S., John Wiley & Sons.

Jones, S.M., Lovell, B. & Crosby, A.G., 2012. Comparison of modern and geological observations of dynamic support from mantle convection, *J. geol. Soc.,* **169,** 745–758.

Jordan, T.H., 1975. The continental tectosphere, *Rev. Geophys. Space Phys.,* **13,** 1–12.

Jordan, T.H., 1978. Composition and development of the continental tectosphere, *Nature,* **274,** 544–548.

Kaban, M., Schwintzer, P. & Reigber, C., 2004. A new isostatic model of the lithosphere and gravity field, *J. Geod.,* **78,** 368–385.

Karato, S.I. & Karki, B.B., 2001. Origin of lateral variation of seismic wave velocities and density in the deep mantle, *J. geophys. Res.,* **106,** 21 771–21 783.

Karato, S.-I. & Li, P., 1992. Diffusion creep in perovskite: implications for the rheology of the lower mantle, *Science,* **255,** 1238–1240.

Karato, S.-i. & Wu, P., 1993. Rheology of the upper mantle: a synthesis, *Science,* **260,** 771–778.

King, S.D., 1995. Radial models of mantle viscosity: results from a genetic algorithm, *Geophys. J. Int.,* **122,** 725–734.

King, S.D. & Hager, B.H., 1994. Subducted slabs and the geoid, 1. Numerical experiments with temperature-dependent viscosity, *J. geophys. Res.,* **99,** 19 843–19 852.

Koptev, A., Ershov, A. & Malovichko, E., 2013. The stress state of the Earth's lithosphere: results of statistical processing of the world stress-map data, *Moscow Univ. Geol. Bull.,* **68,** 17–25.

Kreemer, C., Holt, W.E. & Haines, A.J., 2003. An integrated global model of present-day plate motions and plate boundary deformation, *Geophys. J. Int.,* **154,** 8–34.

Lee, C.-K., Han, S.-C. & Steinberger, B., 2011. Influence of variable uncertainties in seismic tomography models on constraining mantle viscosity from geoid observations, *Phys. Earth planet. Inter.,* **184,** 51–62.

Lithgow-Bertelloni, C. & Gurnis, M., 1997. Cenozoic subsidence and uplift of continents from time-varying dynamic topography, *Geology,* **25,** 735–738.

Lithgow-Bertelloni, C. & Guynn, J.H., 2004. Origin of the lithospheric stress field, *J. geophys. Res.,* **109,** doi:10.1029/2003JB002467.

Liu, X. & Zhong, S., 2015. The long-wavelength geoid from three-dimensional spherical models of thermal and thermochemical mantle convection, *J. geophys. Res.,* **120,** 4572–4596.

Liu, X. & Zhong, S., 2016. Constraining mantle viscosity structure for a thermochemical mantle using the geoid observation, *Geochem. Geophys. Geosyst.,* **17,** 895–913.

Manea, V. & Gurnis, M., 2007. Subduction zone evolution and low viscosity wedges and channels, *Earth planet. Sci. Lett.,* **264,** 22–45.

McKenzie, D., 1977. Surface deformation, gravity anomalies and convection, *Geophys. J. Int.,* **48,** 211–238.

McKenzie, D., 1994. The relationship between topography and gravity on Earth and Venus, *Icarus,* **112,** 55–88.

McNamara, A.K., van Keken, P.E. & Karato, S.-I., 2002. Development of anisotropic structure in the Earth's lower mantle by solid-state convection, *Nature,* **416,** 310–314.

Mitrovica, J. & Forte, A., 2004. A new inference of mantle viscosity based upon joint inversion of convection and glacial isostatic adjustment data, *Earth planet. Sci. Lett.,* **225,** 177–189.

Molnar, P., England, P.C. & Jones, C.H., 2015. Mantle dynamics, isostasy, and the support of high terrain, *J. geophys. Res.,* **120,** doi:10.1002/2014JB011724.

Moresi, L. & Gurnis, M., 1996. Constraints on the lateral strength of slabs from three-dimensional dynamic flow models, *Earth planet. Sci. Lett.,* **138,** 15–28.

Moresi, L. & Parsons, B., 1995. Interpreting gravity, geoid, and topography for convection with temperature dependent viscosity: application to surface features on Venus, *J. geophys. Res.,* **100,** 21 155–21 171.

Moucha, R., Forte, A., Mitrovica, J. & Daradich, A., 2007. Lateral variations in mantle rheology: implications for convection related surface observables and inferred viscosity models, *Geophys. J. Int.,* **169,** 113–135.

Moucha, R., Forte, A.M., Mitrovica, J.X., Rowley, D.B., Quéré, S., Simmons, N.A. & Grand, S.P., 2008. Dynamic topography and long-term sea-level variations: there is no such thing as a stable continental platform, *Earth planet. Sci. Lett.,* **271,** 101–108.

Müller, R.D., Sdrolias, M., Gaina, C. & Roest, W.R., 2008. Age, spreading rates, and spreading asymmetry of the world's ocean crust, *Geochem. Geophys. Geosyst.,* **9,** doi:10.1029/2007GC001743.

Nakiboglu, S., 1982. Hydrostatic theory of the Earth and its mechanical implications, *Phys. Earth planet. Inter.,* **28,** 302–311.

Naliboff, J., Conrad, C. & Lithgow-Bertelloni, C., 2009. Modification of the lithospheric stress field by lateral variations in plate-mantle coupling, *Geophys. Res. Lett.,* **36,** doi:10.1029/2009GL040484.

Panasyuk, S.V. & Hager, B.H., 2000a. Inversion for mantle viscosity profiles constrained by dynamic topography and the geoid, and their estimated errors, *Geophys. J. Int.,* **143,** 821–836.

Panasyuk, S.V. & Hager, B.H., 2000b. Models of isostatic and dynamic topography, geoid anomalies, and their uncertainties, *J. geophys. Res.,* **105,** 28 199–28 209.

Panet, I., Pajot-Métivier, G., Greff-Lefftz, M., Métivier, L., Diament, M. & Mandea, M., 2014. Mapping the mass distribution of Earth's mantle using satellite-derived gravity gradients, *Nat. Geosci.,* **7,** 131–135.

Parsons, B. & Daly, S., 1983. The relationship between surface topography, gravity anomalies, and temperature structure of convection, *J. geophys. Res.,* **88,** 1129–1144.

Pearson, D. *et al.*, 2014. Hydrous mantle transition zone indicated by ringwoodite included within diamond, *Nature,* **507,** 221–224.

Pekeris, C.L., 1935. Thermal convection in the interior of the Earth, *Geophys. J.,* **3,** 343–367.

Peslier, A.H., Woodland, A.B., Bell, D.R. & Lazarov, M., 2010. Olivine water contents in the continental lithosphere and the longevity of cratons, *Nature,* **467,** 78–81.

Press, W.H., Teukolsky, S., Vetterling, W. & Flannery, B.P., 2007. *Numerical Recipes* 3rd Edition: *The Art of Scientific Computing,* Cambridge Univ. Press.

Reguzzoni, M. & Tselfes, N., 2009. Optimal multi-step collocation: application to the space-wise approach for GOCE data analysis, *J. Geod.,* **83,** 13–29.

Ricard, Y., Fleitout, L. & Froidevaux, C., 1984. Geoid heights and lithospheric stresses for a dynamic Earth, *Ann. Geophys.,* **2,** 267–286.

Ricard, Y., Richards, M., Lithgow-Bertelloni, C. & Le Stunff, Y., 1993. A geodynamic model of mantle density heterogeneity, *J. geophys. Res.,* **98,** 21 895–21 909.

Richards, M.A. & Hager, B.H., 1988. The Earth's geoid and the large-scale structure of mantle convection, in *The Physics of Planets*, vol. 1, pp. 247–272, ed. Runcorn, S.K., John Wiley and Sons.

Richards, M.A. & Hager, B.H., 1989. Effects of lateral viscosity variations on long-wavelength geoid anomalies and topography, *J. geophys. Res.,* **94,** 10 299–10 313.

Ritsema, J., Deuss, A., Van Heijst, H. & Woodhouse, J., 2011. S40RTS: a degree-40 shear-velocity model for the mantle from new Rayleigh wave dispersion, teleseismic traveltime and normal-mode splitting function measurements, *Geophys. J. Int.,* **184,** 1223–1236.

Rudolph, M.L., Lekić, V. & Lithgow-Bertelloni, C., 2015. Viscosity jump in Earth's mid-mantle, *Science,* **350,** 1349–1352.

Sambridge, M., 1999. Geophysical inversion with a neighbourhood algorithm—I. Searching a parameter space, *Geophys. J. Int.,* **138,** 479–494.

Sen, M.K. & Stoffa, P.L., 2013. *Global Optimization Methods in Geophysical Inversion,* 2nd edn, Cambridge Univ. Press.

Simmons, N.A., Forte, A.M., Boschi, L. & Grand, S.P., 2010. GyPSuM: a joint tomographic model of mantle density and seismic wave speeds, *J. geophys. Res.,* **115,** doi:10.1029/2010JB007631.

Simons, M., Solomon, S.C. & Hager, B.H., 1997. Localization of gravity and topography: constraints on the tectonics and mantle dynamics of Venus, *Geophys. J. Int.,* **131,** 24–44.

Smith, W.H. & Sandwell, D.T., 1997. Global sea floor topography from satellite altimetry and ship depth soundings, *Science,* **277,** 1956–1962.

Soldati, G., Boschi, L., Deschamps, F. & Giardini, D., 2009. Inferring radial models of mantle viscosity from gravity (GRACE) data and an evolutionary algorithm, *Phys. Earth planet. Inter.,* **176,** 19–32.

Solomatov, V., 1996. Can hotter mantle have a larger viscosity?, *Geophys. Res. Lett.,* **23,** 937–940.

Solomatov, V. & Reese, C., 2008. Grain size variations in the Earth's mantle and the evolution of primordial chemical heterogeneities, *J. geophys. Res.,* **113,** doi:10.1029/2007JB005319.

Spasojevic, S. & Gurnis, M., 2012. Sea level and vertical motion of continents from dynamic earth models since the Late Cretaceous, *AAPG Bull*., **96,** 2037–2064.

Spasojevic, S., Gurnis, M. & Sutherland, R., 2010. Inferring mantle properties with an evolving dynamic model of the Antarctica-New Zealand region from the Late Cretaceous, *J. geophys. Res.,* **115,** doi:10.1029/2009JB006612.

Stadler, G., Gurnis, M., Burstedde, C., Wilcox, L.C., Alisic, L. & Ghattas, O., 2010. The dynamics of plate tectonics and mantle flow: from local to global scales, *Science,* **329,** 1033–1038.

Steinberger, B., 2007. Effects of latent heat release at phase boundaries on flow in the Earth's mantle, phase boundary topography and dynamic topography at the Earth's surface, *Phys. Earth planet. Inter.,* **164,** 2–20.

Stixrude, L. & Lithgow-Bertelloni, C., 2007. Influence of phase transformations on lateral heterogeneity and dynamics in Earth's mantle, *Earth planet. Sci. Lett.,* **263,** 45–55.

Sutherland, R., Spasojevic, S. & Gurnis, M., 2010. Mantle upwelling after Gondwana subduction death explains anomalous topography and subsidence histories of eastern New Zealand and West Antarctica, *Geology,* **38,** 155–158.

Thoraval, C. & Richards, M.A., 1997. The geoid constraint in global geodynamics: viscosity structure, mantle heterogeneity models and boundary conditions, *Geophys. J. Int.,* **131,** 1–8.

Tosi, N., Čadek, O. & Martinec, Z., 2009. Subducted slabs and lateral viscosity variations: effects on the long-wavelength geoid, *Geophys. J. Int.,* **179,** 813–826.

Turcotte, D.L. & Schubert, G., 2014. *Geodynamics,* 2nd edn, Cambridge Univ. Press.

Van Laarhoven, P.J. & Aarts, E.H., 1987. *Simulated Annealing: Theory and Applications,* Vol. 37, Springer Science & Business Media.

Vassiliou, M., Hager, B. & Raefsky, A., 1984. The distribution of earthquakes with depth and stress in subducting slabs, *J. Geodyn.,* **1,** 11–28.

Wheeler, P. & White, N., 2000. Quest for dynamic topography: observations from Southeast Asia, *Geology,* **28,** 963–966.

Wheeler, P. & White, N., 2002. Measuring dynamic topography: an analysis of Southeast Asia, *Tectonics,* **21,** doi:10.1029/2001TC900023.

Whittaker, J.M., Goncharov, A., Williams, S.E., Müller, R.D. & Leitchenkov, G., 2013. Global sediment thickness data set updated for the Australian-Antarctic Southern Ocean, *Geochem. Geophys. Geosyst.,* **14,** 3297–3305.

Winterbourne, J., White, N. & Crosby, A., 2014. Accurate measurements of residual topography from the oceanic realm, *Tectonics,* **33,** 982–1015.

Yang, T. & Fu, R., 2014. Thermochemical piles in the lowermost mantle and their evolution, *Phys. Earth planet. Inter.,* **236,** 109–116.

Yoshida, M. & Nakakuki, T., 2009. Effects on the long-wavelength geoid anomaly of lateral viscosity variations caused by stiff subducting slabs, weak plate margins and lower mantle rheology, *Phys. Earth planet. Inter.,* **172,** 278–288.

Zhong, S. & Davies, G.F., 1999. Effects of plate and slab viscosities on the geoid, *Earth planet. Sci. Lett.,* **170,** 487–496.

Zhong, S. & Gurnis, M., 1992. Viscous flow model of a subduction zone with a faulted lithosphere: long and short wavelength topography, gravity and geoid, *Geophys. Res. Lett.,* **19,** 1891–1894.

Zhong, S. & Gurnis, M., 1994. Role of plates and temperature-dependent viscosity in phase change dynamics, *J. geophys. Res.,* **99,** 15 903–15 917.

Zhong, S., Zuber, M.T., Moresi, L. & Gurnis, M., 2000. Role of temperature-dependent viscosity and surface plates in spherical shell models of mantle convection, *J. geophys. Res.,* **105,** 11 063–11 082.

Zoback, M.L., 1992. First-and second-order patterns of stress in the lithosphere: the world stress map project, *J. geophys. Res.,* **97,** 11 703–11 728.